Computational study of vortex shedding behind bluff bodies

Brice Vallès

Department of Applied Mechanics,
Thermodynamics and Fluid Dynamics
Norwegian University of Science and Technology

October 8, 2001

Summary

A computational study of vortex shedding behind bluff bodies is presented. The main focus of this work is the study of vortex shedding and wake flow behaviour behind tapered circular cylinders in the laminar flow regime. However, a stepped circular cylinder in laminar flow as well as uniform circular cylinders in the turbulent flow regime have been investigated as well.

In the laminar flow regime, the flow behaviour behind tapered and stepped circular cylinders is rather different than behind a uniform circular cylinder. Because the tapered and the stepped circular cylinders are three-dimensional objects, as opposed to uniform circular cylinders which are nominally two-dimensional, secondary flows are generated along the cylinder span causing complex three-dimensional flow patterns which are still not completely understood. The main motivation of the thesis is thus to contribute to improve knowledge of vortex shedding phenomena.

This thesis is consists of two main parts. Firstly, a brief description of the work is given, as well as the numerical tools used, the vortex shedding phenomenon in laminar and turbulent flow regimes. In addition, some of the results are presented. Secondly, the appendices in which published and submited papers on the subject are enclosed. The aim of the first part is to provide details and/or questions which are not included in the latter papers in order to form a more comprehensive document.

Preface

Vortex shedding behind bluff bodies was a completely new field of investigation for me when I first started this doctoral thesis. After three years of challenging, exciting, and pleasant research, I hope this thesis will help the reader, specialized or not in vortex shedding, to have a better understanding of the complex wake-flow occuring behind bluff bodies. Because this manuscript is destined to a broad audience, the writing style is of two sorts: a scientific style has been used for the papers placed in the appendices, whereas a more popularization style has been used for the first main part of the present document.

This project has received support from The Research Council of Norway (Programme for Supercomputing) through a grant of computing time. This work was also funded by The Research Council of Norway under contract no. 121279/410.

I am grateful to Professor Peter K. Stansby, Professor Arne E. Holdø and Professor Bjørnar Pettersen for having accepted to evaluate this doctoral thesis.

This doctoral thesis would have been impossible to do without the advices and guidance of my two supervisors, Professor Helge I. Andersson and Dr. Ing. Carl B. Jenssen. Their patience, knowledge and friendship have been highly appreciated. I am really grateful to them for having taking the risk to hire a frenchman who had never been in Norway before.

I would like to thank the "Ph. D. family", made up of the doctoral students of the "MTF" department, with whom I now share wonderful memories. My gratitude to Gerda Nubdal and Elisabeth Hovda who helped me in learning norwegian. Thanks to the latter one who had to share the office and to stand a somewhat noisy frenchman from Marseille.

I am really grateful to Associate Professor Reidar Kristoffersen, the cornerstone of the "Ph. D. family", whose kindness and scientific skills helped me throughout these three years.

Thanks are also due to Vanessa Hagen for helping me proofreading this manuscript.

I would also like to thank the swimmers, trainer Elena Forbregd, and all the members of the Vestbyen IL Svømming club who welcomed me and allowed me to practice swimming; perhaps the best sport for a fluid mechanician.

Thanks to all the members of the "Trondheim Kamera Klubb", and especially to Alberto Commodaro, with whom I share the passion for taking pictures. Being a photographer helps me to observe my surrounding and consequently the phenomena of nature.

Finalement, je tiens tout particulièrement à remercier mes parents, Philippe et Mireille Vallès, sans qui, après tout, cette thèse n'existerait pas. Leur inconditionnel soutien tout au long de ces années d'études est simplement sans prix. Je voudrais, de la même façon, remercier mon frère, Roch Vallès, qui a toujours su supporter mes décisions quelqu'extravagantes qu'elles pussent être. Cette thèse est leure.

Je tiens également à remercier tous mes grands-parents ainsi que les autres membres de la famille pour la grande ouverture d'esprit dont ils ont fait preuve lors de ma décision d'aller poursuivre mes études dans les lointaines contrées scandinaves.

Trondheim, August 2001

Brice Vallès

Contents

Part I
Introduction

1 Motivation

Take a look around you, what do you see? Many different geometrical shapes. We are living surrounded by objects with different forms. In everyday life, because we are used to these objects, we are not conscious of the fact that they have usually been designed and built on purpose. In engineering, the shape of the objects is especially important and miscalculations or lack of knowledge can lead to great disasters. One of the most famous examples of an engineering failure is the spectacular collapse of the "Tacoma Narrows Bridge". The bridge was of an unusually light design, peculiarly sensitive to high winds. Rather than resist the forces of the wind, it tended to sway and vibrate. Unfortunately, this was discovered too late. On November 7, 1940, in a 64-kilometer-per-hour wind, the center span began to sway and vibrate, then twist. The combined forces of the wind and the internal stress was too great for the bridge, and it self-destructed. It is important to know the reasons why such catastrophes happen in order to prevent similar failures in the future. There are two complementary ways to do so: risks analysis and academic studies. The former investigates the risks of existing systems to be destroyed or damaged by any possible effects, as well as the consequences of the resulting damages. The latter is devoted to improving the knowledge of the physical phenomena which could cause, contribute to, or originate such disasters. The project presented here is in keeping with this more academic investigation.

Why should one spend time on studying, by means of numerical methods, the shedding of vortices behind bluff bodies rather than another physical problem? This question is twofold. Firstly, why study the shedding of vortices? Besides the fact that it is an interesting and complex phenomenon, it can be one of the physical phenomena leading to engineering failures. Indeed, Theodore von Kármán, who studied the collapse of the Tacome bridge, was the first to associate this collapse with the periodic shedding of vortices which frequency matching the bridge resonance frequency. Secondly, why "behind bluff bodies"? To answer this, we need to know what "bluff body" means. As defined by Zdravkovich [1] (page 3), "bluff bodies may have sharp edges on their circumferences, such as flat plates, triangular, rectangular, and polygonal cylinders, or may be rounded like circular, elliptical, and arbitrary oval cylinders". One of the main difficulties in studying flow over round edges is that the flow separation points are not fixed (as is usually the case with sharp edges), but can move in response to the flow structure in the separated region. Today, based on theoretical studies, experiments, and numerical simulations, the behaviour of the flow around a uniform circular cylinder and the vortex-shedding phenomenon occurring in its wake flow are quite well known for any kind of Reynolds number [1, 2]. Surprisingly, few studies can be found in literature on other types of circular cylinders such as stepped or tapered circular cylinders, despite their obvious industrial use (pillars of offshore plateforms, factory chimneys). This is probably due to the fact that these three-dimensional objects give rise to a different and much more complex three-dimensional wake than a nominally two-dimensional uniform circular cylinder. Because of this lack of knowledge, it has been found interesting to investigate the vortex shedding behind stepped and tapered circular cylinders, thereby contributing to a better

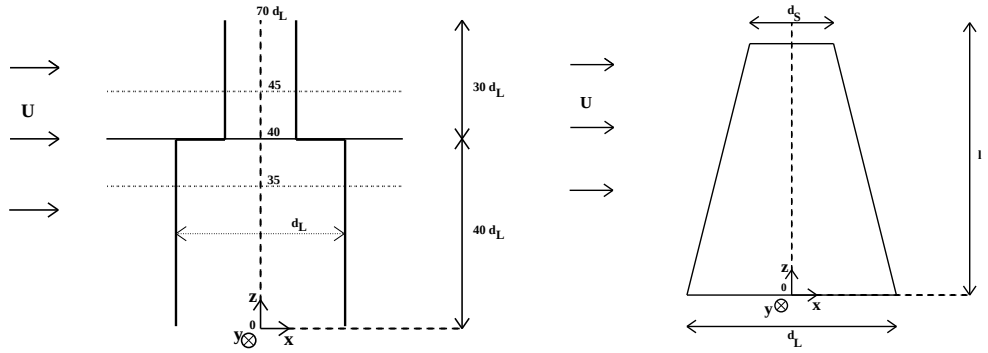

Figure 1: Sketch of the bluff-body geometries: (a) stepped circular cylinder, (b) tapered circular cylinder.

understanding of this phenomenon. Today, with the present computer capabilities, it has become possible to study such cases numerically. Among other advantages, numerical simulations are cheaper and easier to perform than experimental investigations. Moreover, simulations provide important supplementary information not readily accessible in laboratory (such as vorticity). Hence, all these different reasons formed the motivations of the present project: "computational simulation of vortex shedding behind bluff bodies".

2 Description

2.1 Proposal

In the original proposal to The Research Council of Norway for funding of this project, the stated aim of this work was to perform numerical simulations behind two different infinitely long stepped circular cylinders and three different linearly tapered circular cylinders. A stepped circular cylinder can be regarded either as a uniform circular cylinder with a sudden change in diameter, or two uniform circular cylinders piled up one on the other (see Figure 1(a)). A linearly tapered cicular cylinder is a circular cylinder with a constant change of diameter all along the spanwise direction (see Figure 1(b)). The stepped cylinder is characterized by its diameter ratio $r = d_L/d_S$, whereas the taper ratio $R_T = l/(d_L - d_S)$ characterizes the tapered cylinder. Here, l is the length of the cylinder, while d_L and d_S denote respectively the large and small diameters. Then, based on the large diameter, the Reynolds number is defined as: $Re_{d_L} = U.d_L/\nu$ where U is the uniform incoming flow velocity and ν is the kinematic viscosity of the fluid. Although these two bluff-body geometries are not too different from the classical uniform circular cylinder, each configuration has its own typical wake-flow behaviour.

In the proposal, both laminar and turbulent flow regimes were under consideration. Firstly, laminar flow past the five different stepped or tapered cylinders was to be studied.

Table 1: Laminar flow: simulations set-up

Stepped Cylinder	r	Re_{d_L} [a]	d_S/d_L	l_L/d_L [b]	l_S/d_L [c]
	1.34	99	0.747	40	35
	R_T	Re_{d_L} [a]	d_S/d_L	l/d_L	Case
Tapered Cylinders	100:1	178	0.625	37.473	A
	75:1	131	0.556	33.461	B
	75:1	163	0.556	33.461	C

[a] $Re_{d_L} = U.d_L/\nu$, i.e. Reynolds number based on the largest diameter
[b] l_L: length of the large diameter part
[c] l_S: length of the small diameter part

For laminar flow, the vortex shedding phenomenon is particularly amenable to detailed investigations, since the time-dependent flow field can be computed by the numerical solution to the Navier-Stokes equations without any semi-empirical turbulence model. After validation of the computational results against experimental data, the proposal called for a more thorough analysis in order to learn more about this particular flow. Secondly, turbulent flow past the same objects was to be simulated. This would have been accomplished by means of large-eddy simulation rather than with the help of turbulence models based on Reynolds Averaged Navier-Stokes (RANS) equations because the inherent averaging procedure is not directly applicable to unsteady flows, and the method does not utilize the potential of finer grids to enhance the resolution of turbulent quantities. Similar in spirit to Direct Numerical Simulation (DNS), Large Eddy Simulation (LES) is based on simulating the turbulent fluctuations that can be resolved in the mesh as an integral part of the flow solution. Only turbulent fluctuations with a length scale smaller than the grid spacing is modeled. Instead of an averaging procedure as in RANS, a Sub Grid Scale (SGS) model is introduced to account for the turbulent motion too small to be captured by the grid resolution. In addition to the possibilities for more accurate simulation of turbulent flows, LES also offers the advantage of producing more information about the flow field, as no averaging procedure is applied to large scale turbulent structures. The SGS models to be used for these tasks were the Smagorinsky model and a dynamic model (see for example [3, 4] for details), the latter was to be implemented during the project. The aim of a dynamic model is to circumvent the problem of choosing the constant which enters into the Smagorinsky model. However, before performing simulations of the turbulent flow past these five cylinder shapes, a uniform circular cylinder was prescribed as a test case in order to validate the different SGS models. The choice of a uniform circular cylinder is justified by the plethora of results available in the literature for turbulent flows around this configuration.

2.2 Project

When one decides to undertake a doctoral thesis, one must be aware that one will certainly encounter many difficulties which can impede and/or prevent the achievement of some of the original aims, as well as realize that some of the proposed investigations are not feasible. This doctoral thesis is not an exception.

For the laminar flow regime, numerical simulations of vortex shedding behind three

Table 2: Turbulent flow: simulations set-up

Uniform	Re_d			l/d
Cylinder	3900			3
Tapered	R_T	Re_{d_L} [a]	d_S/d_L	l/d_L
Cylinder	51.3:1	3900	0.822	9.112

[a] $Re_{d_L} = U.d_L/\nu$, i.e. Reynolds number based on the largest diameter

different circular cylinders have been performed: one stepped circular cylinder (see Appendix A) and two tapered circular cylinders (see Appendixes B and C). The different configurations, as shown in Table 1, have been chosen in order to fit the experiments of Lewis & Gharib [5] on stepped circular cylinders and Piccirillo & Van Atta [6] on tapered circular cylinders. For an exact reproduction of the experiments [5] the length ratios l_L/d_L and l_S/d_L of the stepped circular cylinder given here (cf. Table 1), should both have been equal to 145. This would have required a computational grid far too big in terms of cpu-time consumption and computer storage even with todays computer capabilities. According to the experimental results [5], the effect of the step on the wake is quite limited in the spanwise direction and does not spread more than about $25d_L$ from the step towards both the large and small diameter parts of the cylinder (see Appendix A). Hence, the use of the present geometry is justified. On the other hand, the three computer simulations of flow past tapered circular cylinders reproduced exactly the experimental geometries used by Piccirillo & Van Atta (1993). The present cases denoted: Case A, Case B and Case C in Table 1, represent the experiments labeled Run 14, Run 22 and Run 23 in reference [6], respectively (see Appendix C).

For the turbulent flow regime, only the test case defined earlier as the simulation of the flow past a uniform circular cylinder, and a single tapered circular cylinder have been studied (see Appendix D). As in the laminar case, the geometries have been carefully chosen (shown in Table 2) to fit other studies (see Appendix D). Because many experimental and DNS results are available for flow around a uniform circular cylinder at $Re = 3900$ (see for example [2, 7] and [8], respectively) this was found to be the best choice for LES validation. On the other hand, the tapered circular cylinder case reproduced one of the experiment done by Hsiao & Chiang [9] except for a slight difference in Reynolds number between the numerical and the experimental studies, $Re = 3900$ instead of 4000 in [9]. According to the existing results for uniform circular cylinders, $Re = 3900$ is quite far from a critical value corresponding to a transition between two flow regimes [1]. A flow regime is when a distinct flow pattern with a limited variation persists over a range of Reynolds numbers. Both $Re = 3900$ and $Re = 4000$ are in the range $10^3 - 2 \cdot 10^3 < Re < 20 \cdot 10^3 - 40 \cdot 10^3$ corresponding to the second phase of the so-called "Transition-in-shear-layers" flow regime [1]. Based on these observations and on the study done by Hsiao & Chiang [9], it has been assumed that the flow regime for tapered circular cylinders at $Re = 3900$ and $Re = 4000$ will be identical. As a result, not only were comparisons between numerical and experimental results possible, but comparisons between simulations for uniform and tapered circular cylinders at identical Reynolds numbers could be made as well.

Firstly, however, it was found advantageous to perform two-dimensional numerical

simulations of flow past circular cylinders. These allowed us to estimate optimum values of different parameters such as time step, convergence criterion, as well as ratios such as mesh size/cpu-time or accuracy/cpu-time (see Section IV and Appendix B). These tests turned out to be of great help because almost no further initial tests were needed when three-dimensional simulations were performed.

Chronologically, tapered circular cylinders were investigated first (see Appendixes B and C). Here, some difficulties in programming or modifying post-treatment softwares were encountered. Hence, because more time than expected was used, and because all the main features of the flow behaviour behind tapered circular cylinders apparently were successfully reproduced, it was decided to move directly to the simulation of flow behind a stepped circular cylinder rather than to carry out a simulation of a third tapered circular cylinder.

The main problem with the simulation of the stepped circular cylinder was the high cpu-time consumption. As shown in Table 1, the dimensions of the stepped cylinder are much larger than the tapered cylinders considered. Thus, the stepped cylinder mesh is larger than these for the tapered cylinders, and the more nodes a grid has, the more cpu-time is required. Then, with the lack of time a dilemma occured: should a complete investigation of this geometry be done in order to attempt to reproduce all the characteristics of the flow described by Lewis & Gharib [5], or should the feasibility of performing LES of turbulent flow be studied? The second alternative was chosen. Consequently, only a single stepped circular cylinder case was reproduced (see Appendix A).

Even if large-eddy simulations allow to use less grid points than DNS, a very fine mesh is needed to get detailed turbulent structures. With 2.4 million points, the second test case (see Appendix D) almost reached the Cray T3E capabilities. The tapered circular cylinder being three times bigger than the uniform circular cylinder, a grid with 7.2 million points was needed to get same accuracy. Fortunately, another computer, the SGI Super-Origin 3800 became available. The change of computer led to the implementation and testing of the code on the new machine. The resulting delays and the long time (both cpu and wall clock time) required by the simulation to be achieved did only allow the study of a single tapered circular cylinder. Large eddy simulation of a stepped circular cylinder being, at that time, an utopia. This is also the reason why only Smagorinsky sub-grid scale model has been tested and no Dynamic model implemented.

Part II
Numerical Tools

Before presenting the results obtained, a brief description of the numerical tools used is provided.

1 Computers

Several computers have been used for different purposes. A Silicon graphics (SGI) Irix64 release 6.5 workstation with four 75 Megahertz (MHz) processors and 512 Megabytes

(MB) Random Access Memory (RAM) was used to create the grids.

The flow simulations were run on two super-computers located at the Norwegian University of Science and Technology (Norges Teknisk-Naturvitenskapelige Universitet). Firstly, a Cray T3E consisting of 96 DEC alpha EV5 processors. Each running at 300 MHz and containing 128 MB RAM. Secondly, a Super Origin 3800 consisting of 220 PEs at 400 MHz with 1000 MB RAM.

The visualizations were performed on a Personal Computer (PC), consisting of one Intel Pentium II processor at 450 MHz and 768 MB RAM.

2 Software

The grid generator called Omega used to create the grids was developped at NTNU by H. Holm. Using OpenGL interface available on the SGI Irix machine, Omega is an interactive program for multiblock mesh generation. The procedure is decomposed into six steps. First, an input file including the coordinates of the basic geometry such as a cylinder for example, is read. Then the user plots the nodes which will form the "corners" of the blocks. The next two steps consist of defining: i/ the lines, or more exactly the segments, delimited by two neighbouring nodes ii/ the patches or surfaces using four connected lines. Then, the hexahedral blocks are defined by three pairs of patches. Finally, depending on the code used for the simulations the format in which the mesh will be written and the type of grid boundaries (no slip, slip, far field conditions) must be chosen.

All visualizations of the results have been made with the commercial software GLview, a registered trademark of ViewTech AS [1]. Glview is a three-dimensional visualization program using the graphic standard OpenGL. GLview requires at least two different files written in a specific format. The first one includes the coordinates and the nodes connexion table of the mesh. The second or other files concern the results which can be scalars or vectors. The size of the latters files being equal to the number of nodes defining the mesh. Then, results can be plotted on the mesh boundaries or visualized in cutting-planes. Isosurface value of scalar results can be shown as well. Moreover, animations are easily made if several result files of the same type are available. For instance, if several result files for the pressure of a time-dependent flow simulation are obtained, one per time step for example, animations of the time evolution of the pressure behaviour on mesh boundaries or inside the mesh (cutting-planes, isosurface values) can be created.

All figures appearing in the appendixes have been produced with GLview. All drawings (except hand drawings in Appendix C) have been made with the free software XFIG available on UNIX system. All curves have been plotted with the free software XMGR except Figure 3 in Appendix C and Figure 2 in Appendix A where a free version of the commercial software MATLAB has been used. Both programs were available on UNIX system.

3 Concurrent Block Jacobi

The code used to perform numerical simulations of flow past stepped or tapered circular cylinders is called "Concurrent Block Jacobi" (CBJ). It was originally developed and

[1] http://www.viewtech.no

implemented by Carl Birger Jenssen as part of his doctoral thesis [10] and has later been extensively modified at CERFACS [2] and SINTEF.

CBJ is a parallel implicit multiblock time-accurate Navier-Stokes solver, using a coarse grid correction scheme (CGCS), based on the Finite Volume Method. The code consits of a rather short main program and a large set of subroutines which encapsulate every basic operation. Thus, all occurences of an operation in the entire program can be modified just by making changes in a single subroutine, while leaving the rest of the program unchanged. To facilitate future changes in the program, the different parts of the algorithm, such as the calculation of inviscid or viscous numerical fluxes, the imposing of boundary conditions, and the solution to the linear system are written in separate subroutines. This has also been done so that these subroutines are based on the governing equations in a form as general as possible.

3.1 Governing Equations

The governing equations are the Navier-Stokes equations. These equations can be written in several ways, for example in conservative form:

$$\begin{cases} \frac{\partial \rho}{\partial t} + \frac{\partial \rho u_i}{\partial x_i} = 0 & \text{Continuity} \\ \frac{\partial \rho u_i}{\partial t} + \frac{\partial \rho u_j u_i}{\partial x_j} = \rho f_i - \frac{\partial P}{\partial x_i} + \mu \frac{\partial^2 u_i}{\partial x_j^2} + (\lambda + \mu) \frac{\partial^2 u_j}{\partial u_i \partial uj} & \text{Momemtum} \\ \frac{\partial \rho E}{\partial t} + \frac{\partial}{\partial x_i} \left((\rho E + P) u_i - k \frac{\partial T}{\partial x_i} - (\mu (\frac{\partial u_j}{\partial x_i} + \frac{\partial u_i}{\partial x_j}) + \lambda (\frac{\partial u_i}{\partial x_i})) u_j \right) = W_f + q_H & \text{Energy} \end{cases} \tag{1}$$

$\forall i$ and $\forall j$ such that $i \in \{1,2,3\}$ and $j \in \{1,2,3\}$. Here, the Einstein convention has been used so that whenever the same index appears twice in any term, summation over the range of that index is implied. For example in the continuity equation: $\frac{\partial \rho}{\partial t} + \frac{\partial \rho u_i}{\partial x_i} = \frac{\partial \rho}{\partial t} + \frac{\partial \rho u}{\partial x} + \frac{\partial \rho v}{\partial y} + \frac{\partial \rho w}{\partial z} = 0$ where x_i (i=1, 2, 3) or (x, y, z) are the Cartesian coordinates and u_i or (u, v, w) are the Cartesian components of the velocity. In Equation 1, t is the time, ρ is the density, E is the total energy per unit mass given by $E = e + \frac{1}{2}(u^2 + v^2 + w^2)$, where e is the internal energy per unit mass. f_i are the Cartesian components of the external forces and W_f the work performed by these external forces. q_H denotes the heat sources. μ is the dynamic viscosity of the fluid. The kinematic viscosity ν introduced in the definition of the Reynolds number in Part I Section 2.1 is equal to: $\nu = \mu/\rho$. λ and μ are related by the Stoke's relation:

$$2\mu + 3\lambda = 0 \tag{2}$$

The CBJ solver has been written for an ideal gas. Hence, in the energy equation (Equation 1), T denotes the absolute temperature defined by

$$T = e \frac{\gamma - 1}{R} \tag{3}$$

where R is the gas constant. In this work, however, μ is constant based on the specified Reynolds number. Defining the specifics heat at constant pressure and constant volume c_P and c_V, respectively, the coefficient γ is defined by: $\gamma = c_P/c_V$. In Equation 1, k

[2] Centre Européen de Recherche et de Formation Avancée en Calcul Scientifique

is the thermal conductivity coefficient, $k = \rho\ c_P \chi$ where χ is the thermal diffusivity coefficient which must be defined empirically. k can be expressed in terms of the Prandtl number P_r: $k = \frac{\gamma}{\gamma-1}\frac{R}{P_r}\mu$. For air at standard conditions $\gamma = 1.4$, $R = 287 m^2/(s^2 K)$ and $P_r = 0.72$.

The term P appearing in Equation 1 is the pressure related to ρ and e by the equation of state:

$$P = (\gamma - 1)\rho e \tag{4}$$

Although CBJ is a compressible code, it has been theoretically shown that for very low Mach numbers, the flow can be considered incompressible. Usually, the criterion applied is: $\frac{1}{2}M^2 < 0.05$, where M is the Mach number (see [11] page 10). Then, for $M \leq 0.31$ the flow can be considered incompressible. Consequently, the value of the Mach number has been fixed to $M = 0.2$ for all the numerical simulations of the present work. Jenssen and Weinerfelt [12] showed that CBJ with $M = 0.2$ reproduced accurately experimental data and computations done by other authors for incompressible flows.

Finite volume formulation implies the use of the integral form of the Navier-Stokes equations. Assuming no external forces or heat sources and a Newtonian fluid, the following condensed form of Equation 1 is obtained:

$$\frac{\partial}{\partial t}\int\int\int_{V(t)} U dV + \int\int_{S(t)} \vec{F}\cdot\vec{n} dS = 0 \tag{5}$$

where U denotes the conserved variables:

$$U = \begin{pmatrix} \rho \\ \rho u \\ \rho v \\ \rho w \\ \rho E \end{pmatrix} \tag{6}$$

$\vec{F}$ is the flux vector and $\vec{n}$ the outwards pointing normal vector to the surface $S(t)$ enclosing the arbitrary volume $V(t)$. The flux vector can be seen as the summation of two parts, a convective ($\vec{F}_C$) contribution and a diffusive ($\vec{F}_D$) contribution also called inviscid and viscous contributions (see for example [13] pp.597-599). Then, Equation 5 becomes:

$$\frac{\partial}{\partial t}\int\int\int_{V(t)} U dV + \int\int_{S(t)} \vec{F}_C\cdot\vec{n} dS - \int\int_{S(t)} \vec{F}_D\cdot\vec{n} dS = 0 \tag{7}$$

From Equation 1, the components of $\vec{F}_C$ and $\vec{F}_D$ are:

$$F_{C_i} = \begin{pmatrix} \rho u_i \\ \rho u_i u_j + P\delta_{ij} \qquad {\scriptstyle j=1\ldots3} \\ (\rho E + P)u_i \end{pmatrix} \qquad i = 1\ldots3 \tag{8}$$

$$F_{D_i} = \begin{pmatrix} 0 \\ \mu\left(\frac{\partial u_i}{\partial x_j} + \frac{\partial u_j}{\partial x_i}\right) + \lambda\left(\frac{\partial u_j}{\partial x_j}\right)\delta_{ij} \qquad {\scriptstyle j=1\ldots3} \\ \mu\left(\frac{\partial u_i}{\partial x_j} + \frac{\partial u_j}{\partial x_i}\right)u_j + \lambda\left(\frac{\partial u_j}{\partial x_j}\right)u_i + k\frac{\partial T}{\partial x_i} \end{pmatrix} \qquad i = 1\ldots3 \tag{9}$$

If n_x, n_y, n_z are the cartesian components of the normal vector and if $v_n = u \cdot n_x + v \cdot n_y + w \cdot n_z$ denotes the velocity component along $\vec{n}$, then $\vec{F}_C \cdot \vec{n}$ becomes:

$$\vec{F}_C \cdot \vec{n} = \begin{pmatrix} \rho v_n \\ \rho u v_n + P n_x \\ \rho v v_n + P n_y \\ \rho w v_n + P n_z \\ (\rho E + P) v_n \end{pmatrix} \tag{10}$$

Introducing the following primitive variables V:

$$V = \begin{pmatrix} \rho \\ u \\ v \\ w \\ P \end{pmatrix} \tag{11}$$

and applying the chain rule to express all derivatives of $\vec{F}_D$ (Equation 9) in terms of derivatives of the primitive variables (Equation 11), $\vec{F}_D \cdot \vec{n}$ becomes:

$$\vec{F}_D \cdot \vec{n} = A_{n,i} \frac{\partial V}{\partial x_i} \tag{12}$$

The three coefficient matrices being:

$$A_{n,x} = \begin{pmatrix} 0 & 0 & 0 & 0 & 0 \\ 0 & (2\mu + \lambda) n_x & \mu n_y & \mu n_z & 0 \\ 0 & \lambda n_y & \mu n_x & 0 & 0 \\ 0 & \lambda n_z & 0 & \mu n_x & 0 \\ k n_x \frac{\partial T}{\partial \rho} & (2\mu u n_x + \lambda v_n) & \mu(v n_x + u n_y) & \mu(w n_x + u n_z) & k n_x \frac{\partial T}{\partial P} \end{pmatrix} \tag{13}$$

$$A_{n,y} = \begin{pmatrix} 0 & 0 & 0 & 0 & 0 \\ 0 & \mu n_y & \lambda n_x & 0 & 0 \\ 0 & \mu n_x & (2\mu + \lambda) n_y & \mu n_z & 0 \\ 0 & 0 & \lambda n_z & \mu n_y & 0 \\ k n_y \frac{\partial T}{\partial \rho} & \mu(u n_y + v n_x) & (2\mu v n_y + \lambda v_n) & \mu(w n_y + v n_z) & k n_y \frac{\partial T}{\partial P} \end{pmatrix} \tag{14}$$

$$A_{n,z} = \begin{pmatrix} 0 & 0 & 0 & 0 & 0 \\ 0 & \mu n_z & 0 & \lambda n_x & 0 \\ 0 & 0 & \mu n_z & \lambda n_y & 0 \\ 0 & \mu n_x & \mu n_y & (2\mu + \lambda) n_z & 0 \\ k n_z \frac{\partial T}{\partial \rho} & \mu(u n_z + w n_x) & \mu(v n_z + w n_y) & (2\mu w n_z + \lambda v_n) & k n_z \frac{\partial T}{\partial P} \end{pmatrix} \tag{15}$$

In CBJ, the inviscid and viscous fluxes are programmed as defined by Equations 10 to 15.

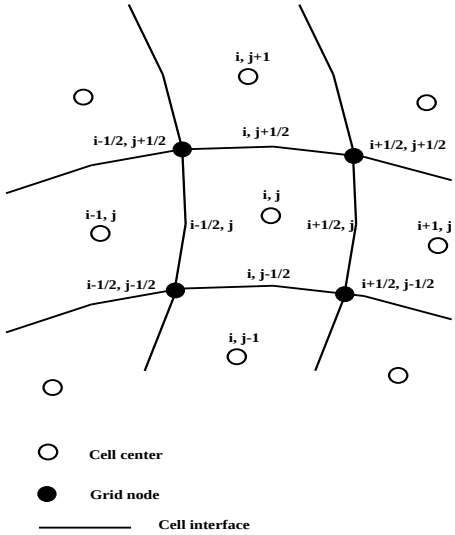

Figure 2: Numbering of nodes, cell centers and cell interfaces in a two-dimensional view of the computational mesh.

3.2 Discretization

The governing equations are discretized in space using a cell centered finite volume method on a conventional multiblock structured mesh. In the finite volume formulation, the discretization is performed on the conservative form of the system of governing equations so that the resulting difference equations remain conservative. For the viscous fluxes, derivatives of second-order accuracy are first calculated with respect to the grid indices, and then transformed to derivatives with respect to the physical spatial coordinates (x, y, z) by means of the chain rule.

On the computational mesh, Equation 5 is applied to hexahedrons with corners defined by intersecting mesh lines. As shown in Figure 2, the cells are numbered by triplets (i, j, k) corresponding to their positions along the axes of the curvilinear coordinate system. $V_{i,j,k}$ denotes the volume of the cell (i, j, k). The cell interfaces are described by $(\vec{n}\ S)_{i\pm\frac{1}{2},j,k}$, $(\vec{n}\ S)_{i,j\pm\frac{1}{2},k}$ and $(\vec{n}\ S)_{i,j,k\pm\frac{1}{2}}$ where the various $\vec{n}$ are the vectors normal to the surfaces of the cell interfaces, and S the surface area of the cell interfaces. The corners of a hexahedron are the points that make up the mesh. Their cartesian coordinates are: $x_{l,i\pm\frac{1}{2},j\pm\frac{1}{2},k\pm\frac{1}{2}}$ $(l = 1 \ldots 3)$. Then, Equation 5 applied to $V_{i,j,k}$ becomes:

$$V_{i,j,k}\frac{\partial}{\partial t}U_{i,j,k} + \sum_{l}\vec{F}_l \cdot (\vec{n}\ S)_l = 0 \tag{16}$$

with $U_{i,j,k}$ the cell average of U and $\vec{F}_l$ the numerically approximated flux through $\vec{n}_l S$, the summation being over $l = (i \pm \frac{1}{2}, j, k), (i, j \pm \frac{1}{2}, k), (i, j, k \pm \frac{1}{2})$.

As mentioned in Appendix B, the convective part of the fluxes is discretized with a third-order, upwind-biased method based on Roe's scheme. The viscous fluxes are obtained using central differencing. Implicit and second-order-accurate time stepping

is achieved by a three point, A-stable, linear multistep method, usually denoted by backward differenciation [3].

The two parts of the fluxes are treated separately. This technique can be used with explicit or implicit schemes. In CBJ, the resulting linear system is solved with a non-factored iterative ADI (Alternating Direction Implicit) technique. With a non-factored iterative ADI scheme, the linear system remains second-order accurate in time.

The Roe's scheme for a system of non-linear hyperbolic equations in one dimension, is given by:

$$F_{C_{i+\frac{1}{2}}} = \frac{1}{2}\left(F_C(U^-_{i+\frac{1}{2}}) + F_C(U^+_{i+\frac{1}{2}})\right) - \frac{1}{2}\left(A^+_{i+\frac{1}{2}} - A^-_{i+\frac{1}{2}}\right)\left(U^+_{i+\frac{1}{2}} - U^-_{i+\frac{1}{2}}\right) \tag{17}$$

$F_{C_{i+\frac{1}{2}}}$ denotes the convective flux through the surface $(\vec{n}_{i+\frac{1}{2}} \cdot dS)$. $A^{\pm}_{i+\frac{1}{2}}$ is defined by:

$$A^{\pm}_{i+\frac{1}{2}} = R_{i+\frac{1}{2}} \Lambda^{\pm}_{i+\frac{1}{2}} R^{-1}_{i+\frac{1}{2}} \tag{18}$$

where $R_{i+\frac{1}{2}}$ is the right eigenvector matrix of $A_{i+\frac{1}{2}}$ which is the Jacobian matrix of F_C taken at $U_{i+\frac{1}{2}}$. $\Lambda^{\pm}_{i+\frac{1}{2}}$ being the diagonal matrices made up with the positive (+) or negative (-) eigenvalues of $A_{i+\frac{1}{2}}$. The state $U_{i+\frac{1}{2}}$ is given by Roe's Riemann solver defined by the equation:

$$F(U^+_{i+\frac{1}{2}}) - F(U^-_{i+\frac{1}{2}}) = A(U_{i+\frac{1}{2}})(U^+_{i+\frac{1}{2}} - U^-_{i+\frac{1}{2}}) \tag{19}$$

where $A(U)$ is the Jacobian matrix to $F(U)$ (cf. [13] Section 20.5.3).

The first order version of Roe's scheme is obtained by simply setting $U^-_{i+\frac{1}{2}} = U_i$ and $U^+_{i+\frac{1}{2}} = U_{i+1}$. Schemes of higher order are obtained by defining $U^-_{i+\frac{1}{2}}$ and $U^+_{i+\frac{1}{2}}$ by higher order extrapolations. The scheme used here is based on an extrapolation of the characteristic variables. First a forwards and backwards finite difference approximation to the change in the characteristic variable at node i is defined:

$$\begin{aligned} \omega^-_{i+\frac{1}{2}} &= R_i^{-1}(U_{i+1} - U_i) \\ \omega^+_{i+\frac{1}{2}} &= R_i^{-1}(U_i - U_{i-1}) \end{aligned} \tag{20}$$

where $R_i^{-1} = R^{-1}\left(U_i, \frac{1}{2}\left(n_{i-\frac{1}{2}}^{\rightarrow} + n_{i+\frac{1}{2}}^{\rightarrow}\right)\right)$. Extrapolating the characteristic variables and transforming back to conserved variables, the right and left states $U^-_{i+\frac{1}{2}}$ and $U^+_{i+\frac{1}{2}}$ are given by:

$$\begin{aligned} U^-_{i+\frac{1}{2}} &= U_i + R_i\left(\tfrac{1+\phi}{4}\omega^+_{i-\frac{1}{2}} + \tfrac{1-\phi}{4}\omega^-_{i+\frac{1}{2}}\right) \\ U^+_{i+\frac{1}{2}} &= U_i - R_i\left(\tfrac{1+\phi}{4}\omega^-_{i+\frac{1}{2}} + \tfrac{1-\phi}{4}\omega^+_{i-\frac{1}{2}}\right) \end{aligned} \tag{21}$$

where R_i is defined in the same way as R_i^{-1} and ϕ is an accuracy parameter used to control the truncation error and upwind biasing. For example $\phi = -1$ gives a second-order fully upwind scheme and $\phi = 1/3$ gives a third-order upwind biased scheme. All the results of this work have been produced with a third-order scheme.

[3] Note: Equation 3 in Appendix B has a mistake which has been corrected in Equation 3 Appendix D

This extrapolation procedure was implemented as part as a TVD (Total Variation Diminishing) scheme. This TVD scheme was switched off for the present work as the flow was assumed to be incompressible.

The extension to two or three dimensions is uniform forward by applying the one-dimensional scheme independently in each coordinate direction.

The viscous part of the flux $\vec{F}_D \cdot \vec{n}$ defined by Equation 12 can be re-written:

$$\vec{F}_D \cdot \vec{n} = A_{x_l} \frac{\partial \xi_m}{\partial x_l} \frac{\partial V}{\partial U} \frac{\partial U}{\partial \xi_m} \tag{22}$$

ξ_m $(m = 1 \ldots 3)$ being the curvilinear coordinates. Then, the derivatives $\frac{\partial}{\partial \xi_m}$ can be calculated directly on the computational mesh using interpolation and central differencing. For any scalar quantity f, at a surface defined by a constant value $i + \frac{1}{2}$, this gives:

$$\begin{aligned}
\left(\frac{\partial f}{\partial \xi_i}\right)_{i+\frac{1}{2},j,k} &\approx f_{i+1,j,k} - f_{i,j,k} \\
\left(\frac{\partial f}{\partial \xi_j}\right)_{i+\frac{1}{2},j,k} &\approx \frac{1}{4}\left(f_{i,j+1,k} + f_{i+1,j+1,k} - f_{i,j-1,k} - f_{i+1,j-1,k}\right) \\
\left(\frac{\partial f}{\partial \xi_k}\right)_{i+\frac{1}{2},j,k} &\approx \frac{1}{4}\left(f_{i,j,k+1} + f_{i+1,j,k+1} - f_{i,j,k-1} - f_{i+1,j,k-1}\right)
\end{aligned} \tag{23}$$

and similarly for surfaces defined by a constant value $j + \frac{1}{2}$ and $k + \frac{1}{2}$. The metrics $\frac{\partial \xi_m}{\partial x_l}$ are obtained by analytically taking the inverse of the matrix whose elements are $\frac{\partial x_l}{\partial \xi_m}$ $(\forall l, l \in \{1,2,3\}$ and $\forall m, m \in \{1,2,3\})$, which are calculated by central differencing.

The time integration is briefly described in Appendix B Secion 2 and in [12]. It is achieved by a three-point, A-stable linear multistep method. A-stability meaning unconditional stability for any time step size (from [14] page 423). The general form of the time integration used is:

$$(1+\xi)U^{n+1} - (1+2\xi)U^n + \xi U^{n-1} = \Delta t \cdot \left(\theta H^{n+1} + (1-\theta-\phi)H^n - \phi H^{n-1}\right) \tag{24}$$

which represents the most general consistent two-step linear multistep method. H is a non-linear function acting on the vector U originating from the space discretization. Depending on the values of the three parameters (θ, ξ, ϕ), this equation will be of different orders and will correspond to different schemes. A partial list of one- and two- step methods can be found in [14] Table 11.1. The numerical simulations for the laminar cases performed here, were made with a "Backward second-order" scheme: $\theta = 1$, $\xi = 1/2$, $\phi = 0$. However, this scheme was found to damp the solutions of the turbulent cases too much. Therefore, other schemes such as "one-step trapezoidal second-order" have been used for simulations at high Reynolds numbers.

3.3 Boundary Conditions

The boundary conditions can be of three types: slip, no-slip or "far field". They are approximated by extending the computational mesh to include "ghost points" outside the boundaries. Slip condition means that the values of the solution vector at the cell interface are equal to these in the cell itself. No-slip condition is usually encountered with walls. Values in ghost cells are set so that the interpolated solution on the cell interface representing the wall satisfies the boundary conditions. There, $u = v = w = 0$, and

from boundary-layer theory $\frac{\partial P}{\partial n} = 0$ (see [11] for instance). Moreover, for an adiabatic or isothermal wall, the boundary conditions for temperature are defined by: $\frac{\partial T}{\partial n} = 0$ or $T = T_{wall}$. The far field is assumed to start at the limit of the computational mesh in the streamwise and crosswise directions, outside the mesh. In the far field, $U = U_\infty$ is constant. At the interface between the far field and the computational mesh two sorts of boundary conditions are applied: Dirichlet type and Neumann type. For a given scalar a at node i, Dirichlet type implies $a_i = a_\infty$, whereas Neumann type implies $\rho\frac{\partial a_i}{\partial t} = 0$. The Dirichlet and Neumann conditions are applied to the so-called Riemann invariants using the following procedure:

From Equation 7, the one-dimensional Euler equation in integral form can be deduced.

$$\frac{\partial U}{\partial t} + \frac{\partial F_C}{\partial X} = 0 \tag{25}$$

where X denotes the coordinate. This can be written:

$$\frac{\partial U}{\partial t} + A\frac{\partial U}{\partial X} = 0 \tag{26}$$

where $A = \frac{\partial F_C}{\partial U}$. Because $\vec{F}_C \cdot \vec{n}$ is an endomorphism, Equation 26 is an eigenvalue problem. An endomorphism being a linear application of a vector space in itself, usually $\mathbb{R}^4$ (space and time) and $\mathbb{R}^2$ in one-dimension (one space dimension and time). Then, $det\,(A - \lambda I) = 0$ implies λ_k eigenvalues. The eigenvector X_k being associated to the eigenvalue λ_k, such that: $(A)\,(X_k) = \lambda_k X_k$. Moreover, if there is an eigenvectors base then A has a matrix in it which is diagonal:

$$A = L\Lambda L^{-1} \tag{27}$$

L is the matrix of eigenvectors and Λ the diagonal matrix whose elements are the eigenvalues. Then Equation 26 becomes:

$$L^{-1}\frac{\partial U}{\partial t} + \Lambda L^{-1}\frac{\partial U}{\partial X} = 0 \tag{28}$$

Riemann introduced a new set of characteristic variables such as: $\delta W = L^{-1}\delta U$, δW representing an arbitrary variation, either $\partial/\partial t$ or $\partial/\partial X$ of W. Hence, the characteristic form of the one-dimensional Euler equation can be decoupled in the W variables and written as:

$$\frac{\partial W}{\partial t} + \Lambda\frac{\partial W}{\partial X} = 0 \tag{29}$$

The three characteristic variables or Riemann invariants are strictly conserved during their propagation along the characteristics defined by:

$$\begin{array}{c} C_0 : \frac{dx}{dt} = u \\ C_+ : \frac{dx}{dt} = u + c \\ C_- : \frac{dx}{dt} = u - c \end{array} \tag{30}$$

c being the sound velocity and $(u, u + c, u - c)$ the eigenvalues. Then, knowing W the conserved variables U are known and the values in the ghost cells defined. Dirichlet conditions are used for Riemann invariants with negative eigenvalue and Neumann conditions

for Riemann invariants corresponding to positive eigenvalue. The positive direction being out of the domain, so that Dirichlet condition is used for waves traveling into the domain, and Neumann condition for waves traveling outside the domain. The interested reader can read [13] Chapter 16 for further details.

3.4 Miscellaneous

The iterative solution procedure is summarized in Appendix B Section 2. Usually, a maximum of 20 Newton iterations is sufficient to reach the convergence criterion. After each Newton iteration, once a solution in every block is obtained, a Coarse Grid Correction Scheme (CGCS) is used to compensate for treating the block interface conditions in an explicit manner by adding global influence to the solution. This accelerates convergence of the multiblock implicit cheme. Therefore, when using the CGCS, the implicit multiblock scheme can be used to solve time-dependent flow. The CGCS described in [15] is a two-level multigrid algorithm applied to a linear system of equations. The main difference from standard multigrid techniques is that it consists of only one fine and one coarse grid. Moreover, a solver, and not a smoother, is employed both on the coarse grid and in each block of the fine grid. The coarse mesh is built by merging several fine cells together (5 in our cases) in each of the spatial directions. If h denotes the fine mesh and H the coarse mesh, the method can be briefly described as follows. In matrix form the linar system to be solved at each Newton iteration can be written as:

$$A_h \Delta U_h = R_h \tag{31}$$

However, because the coupling between blocks is ignored, an incorrect system is solved. If ε_h denotes the error by solving the incorrect system, $\varepsilon_h = \Delta U_h - \widetilde{\Delta U_h}$ then Equation 31 becomes:

$$A_h \varepsilon_h = R_h - A_h \widetilde{\Delta U_h} \tag{32}$$

As in traditional multigrid methods, restriction (I_h^H) and prolongation (I_H^h) operators are used in the definition of the coarse grid representation. The coarse grid system solved is then

$$A_H \Delta U_H = R_H \tag{33}$$

where $A_H = I_h^H A_h I_H^h$ and $R_H = I_h^H (R_h - A_h \widetilde{\Delta U_h})$. The solution to Equation 33 is transformed to the fine grid by means of I_H^h, and finally the fine grid solution is updated by

$$\widetilde{\widetilde{\Delta U_h}} = \widetilde{\Delta U_h} + I_H^h \Delta U_h \tag{34}$$

It has been shown [15, 12] that the use of a CGC Scheme required three time less cpu-time than a simple block Jacobi method to reach convergence for the same level of accuracy on a representative test case.

Part III
Vortex Shedding

One of the first to describe the vortex shedding phenomenon was Leonardo da Vinci. His sixteenth century drawings of flow fields are well known. In 1911, Theodore von Kármán described a regular vortex-street pattern occuring behind a circular cylinder in laminar flow. The vortex shedding phenomenon has for a long time been a subject of curiosity and great interest in science and engineering. The case which has been most studied is without any controversy the vortex shedding occuring behind a uniform circular cylinder. As the Reynolds number increases (from zero to infinity) several different modes of vortex shedding can be distinguished. As seen in [1] Table 1.1, five different states, each including different regimes of vortex shedding, are defined. Every single regime corresponds to a specific range of the Reynolds number. In order to give a general understanding about what is the vortex shedding phenomenon, a brief description for the case of uniform circular cylinders at the Reynolds numbers studied in this project is provided. These regimes are the third of the "Laminar" state ($30-48 < Re < 180-200$) and the second of the "Transition in Shear Layers" state ($1000-2000 < Re < 20\ 000-40\ 000$) as defined in [1]. In addition, it has been found interesting to generally describe also a third case: an incoming linear shear flow past a uniform circular cylinder. As stated in Appendix C, there are many similarities between a uniform incoming flow past a linearly tapered circular cylinder and an incoming linear shear flow past a uniform circular cylinder. Therefore, the main characteristics of the latter configuration are also provided. A detailed description of the vortex shedding behind stepped and tapered circular cylinders are found herein in the "Results" part and in the Appendices.

1 Periodic Wake Regime of Laminar State

Below $Re = 30$ a steady, elongated and closed near-wake is formed behind the cylinder. The two free shear layers meet at the confluence point thereby forming a "bubble" behind the cylinder; Figure 3(a) provides a sketch of this configuration. At the confluence point the velocity is zero. The bubble is composed by two symmetrically placed vortices on each side of the wake, it is then considered as a region of stagnation flow. Moreover, the trail of the wake does not sway.

When the Reynolds number is increased ($Re \geq 30$), transverse oscillations can be first seen far away from the standing eddies. These oscillations are similar to Tollmien-Schlichting waves. This undulation moves progressively towards the cylinder and its amplitude increases with increasing Reynolds number. Once the total wake (until the confluence point) is swaying, some fluid particles are entering the bubble from the confluence point. Hence, there is a mass transfer, and a back-flow is generated inside the bubble from the confluence point towards the cylinder. This region is then a recirculation region and the two vortices become asymmetric. At $Re = 40$, the width and the length of the recirculation zone are nearly one and two cylinder diameters, respectively. The two asymmetric vortices start to oscillate in turn, while beyond them, each of the separated shear layers alternately rolls up at crests and troughs into opposite vortices. Thus, the two bubble vortices are elongated in turn until their downstream parts detatches. This

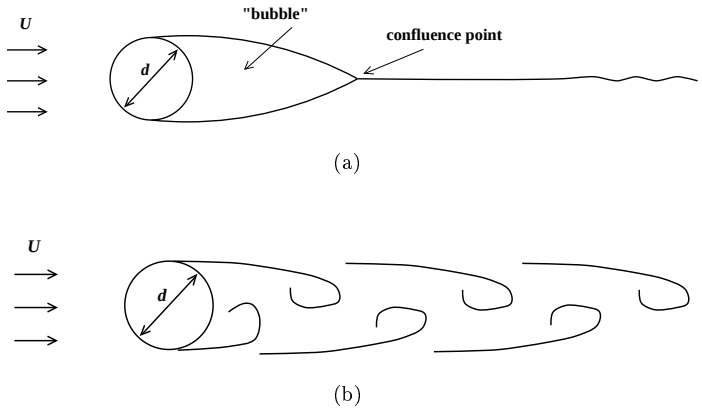

Figure 3: Sketch of vortex shedding in cross sectional view: (a) at $Re < 49$, (b) at $Re > 49$ (Kármán vortex street).

periodically reduces their sizes and leads to the alternate shedding of fluid rotating in opposite directions. Then, the vortices are carried downstream with a speed slightly lower than that of the free stream. Consequently, two stable regular rows of vortices, in staggered arrangement and aligned on each side of the downstream centerline, take place behind the recirculation region. The alternately shed vortices form what is known as the Kármán vortex street, as it is sketched in Figure 3(b). As mentioned by Williamson [16], this results from an absolute instability in the near wake which involves the establishment of the self-sustained oscillation, while further away from the cylinder, a convective instability is found. By definition, a flow is said to be absolutely unstable when "an impulsively generated, small-amplitude transient grows exponentially in place, i.e. at the location of its generation". A convective instability is when the transient is convected downstream leaving the flow at the location of its generation undisturbed. Provansal et al. [17] showed that Kármán vortex shedding from a cylinder was a limit-cycle oscillation of the near wake, resulting from a time-amplified global instability. Moreover, they described the wake dynamics by a Stuart-Landau nonlinear equation. The equation for the complex amplitude used was

$$\frac{dA}{dt} = \sigma A - \lambda |A|^2 A \tag{35}$$

for complex coefficients σ and λ. From stability analysis, Provansal et al. showed that the real part of σ, σ_r, played the role of a Hopf bifurcation parameter, which is equal to zero at $Re = Re_{crit}$ ($Re_{crit} \approx 49$ being the critical value of Reynolds number for which Kármán vortex shedding first occur). They stated that the first order approximation for σ_r and the limit cycle amplitude A followed the laws: $\sigma_r = k(Re - Re_{crit})$ and $A = \alpha(Re - Re_{crit})^{\frac{1}{2}}$ with α and k constants ($k > 0$).

Another important feature of the vortex shedding behind circular cylinders is the existence of two modes of shedding: oblique and parallel. The vortices can be shedded either parallel to the cylinder axis either by forming an angle relatively to the cylidner axis. Williamson [18, 19] showed that these two types of vortex shedding are linked. In

the investigation of circular cylinder wake flows, many authors have noticed the occurence of discontinuities in the Strouhal-Reynolds number relationship. The Strouhal number is a dimensionless frequency defined as: $St = f \cdot d/U$, where d is the cylinder diameter, U the incoming flow velocity and f the vortex-shedding frequency. The inverse of the Strouhal number can be seen as a dimensionless time scale for the vortex shedding phenomenon. The interpretation of the discontinuities gave rise to some debate (see for example the papers of Tritton [20, 21] and Gaster [22, 23]). Williamson [18, 19] showed that with parallel shedding, the Strouhal-Reynolds number curve was completely continuous and that the discontinuities were due to a changeover from one mode of oblique shedding to another oblique mode, as the Reynolds was increased. Moreover, the experimental oblique shedding data could be closely collapsed onto the parallel shedding curve by the use of a simple trigonometric relation:

$$S_{parallel} = S_{oblique}/cos(\theta) \tag{36}$$

where θ is the angle between the shedded vortices and the cylinder axis. This breakthrough led to the definition of a universal Strouhal-Reynolds number curve [18]:

$$St = \frac{A}{Re} + B + C \cdot Re \tag{37}$$

where $A = -3.3265$, $B = 0.1816$ and $C = 1.600 \times 10^{-4}$. As mentioned in Appendix C, in 1998, Williamson & Brown [24] showed that a more accurate $St - Re$ relationship than the one established ten years earlier could be given by:

$$St = A + \frac{B}{\sqrt{Re}} + \frac{C}{Re} \tag{38}$$

where $A = 0.2850$, $B = -1.3897$ and $C = 1.8061$. In the same paper, Williamson & Brown presented another $St-Re$ curve based on DNS computations for two-dimensional laminar shedding over a larger range of Reynolds numbers (up to $Re = 1000$) than is possible to obtain experimentally. As can be seen in Figure 4(a), the three curves are almost not distinguishable. At higher Reynolds numbers, Figure 4(b), a large discrepancy exists between the 1988 relationship and the two others. According to Williamson & Brown [24], the "new" curves accurately represent the experimental data in both laminar and three-dimensional wake turbulent regimes, "although the validity of these representations at these higher Re needs further support". However, these curves do not represent the breakdown of the experimental data curves due to the transition to turbulence occuring in the range $190 < Re < 260$. Above $Re = 190$, the primary shedding vortices become unstable to a spanwise waviness called mode A [25] corresponding with a somewhat lower Strouhal number. Between $Re = 230$ and $Re = 260$ a transition to a mode B occurs, which involves finer-scale streamwise vortices appearing in the near wake.

It has been shown [19] that the particular boundary conditions at the spanwise ends of the cylinder dictate the angle of shedding over the whole span, even for a cylinder with high aspect ratios (length/diameter > 100). Consequently, by manipulating the end conditions, parallel shedding can be achieved. For example, Williamson [19] used endplates whose leading edges were angling inwards, whereas Eisenlohr & Eckelmann [26] used larger coaxial cylinders at the two extremities of the cylinder span. The effect of such

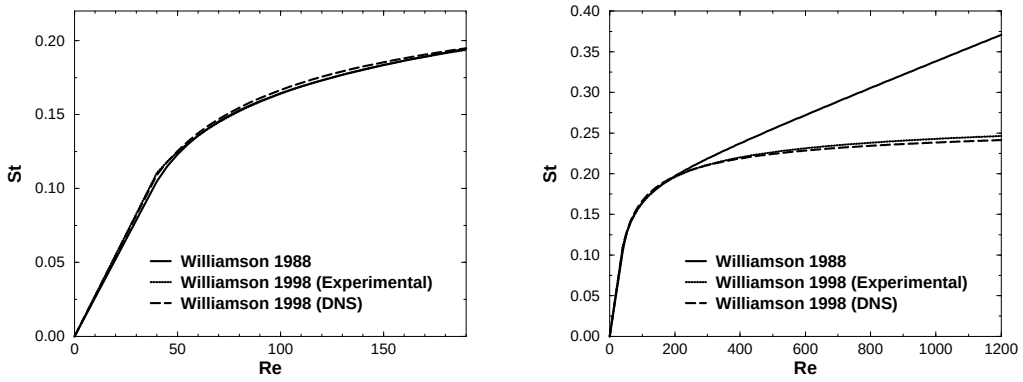

(a) (b)

Figure 4: Strouhal-Reynolds number curves established by Williamson in 1988 and 1998 [18, 24]. (a): close-up in the laminar regime $49 < Re < 190$; (b) comparisons of the curves over a wide range of Reynolds number $49 < Re < 1200$.

techniques is to slightly speed up the flow near the ends. According to Williamson [16], a local incident velocity increase of 1.5% above the free stream velocity can trigger parallel shedding over the whole span. The same results has been shown by Norberg [7] who achieved parallel shedding at very large aspect ratios (length/diameter > 2000).

When there is oblique shedding a cellular structure of the wake in the spanwise direction can be seen. Each cell has one constant vortex-shedding frequency, two neighbouring cells having two different frequencies. At a given Reynolds number, the lowest frequency is found in the cell closest to the ends of the cylinder span. The shedding frequency associated with each cell increases from the end cell to the central cell of the wake. With identical boundary conditions at the two extremities of the cylinder a "chevron" pattern [18, 19] can be observed. At the boundaries between cells, because vortices on each side are moving in and out of phase with each other, vortex dislocation [19] or vortex splitting [26] can occur. Leweke et al. [27] proposed a mechanism for the formation of shedding cells in wakes of uniform circular cylinder at low Reynolds numbers. That is the successive spatial destabilization of oblique shedding patterns by the Eckhaus instability, initiated at the ends of the cylinder span. Eckhaus instability is a secondary instability [28] which renders the oblique vortex shedding unstable, leading to a breakup into cells when the shedding angle exceeds a critical value. A corollary is that the value of the shedding angle is entirely determined by the nature of the end conditions.

Another feature of the uniform circular cylinder wake flow for the periodic wake regime of laminar state occurs above $Re = 100$. In the far wake (100-150 diameters downstream), the vortex street does not remain stable during its downstream development but becomes more and more deformed and breaks down. But, very far away from the cylinder (600 diameters) in the downstream direction, a second regular vortex street with a larger cross

spacing and a much larger wavelength than the first vortex street, appears and persists over a quite long distance (1000 diameters) [1]. This secondary street seems to be due to hydrodynamic instability and no direct relationship should be expected between the frequencies in the primary and secondary regions [16]. According to Williamson [16], the "characteristic that actually forges a connection between the near and far wakes is the sensitivity to free-stream disturbances. The far wake, being a convectively unstable flow, will tend to amplify extremely small frequency peaks in the free".

2 Intermediate Regime of Transition in Shear Layers State

When transition waves, which are second-order instabilities, appear along the free shear layers, three-dimensional vortex interactions and the first manifestation of turbulence occur. Transition eddies are formed as a chain along free shear layers and precede the transtion to turbulence [1]. As a result of the appearance of the transition waves, the vortices convected downstream contain unstable fluid which become progressively turbulent under the influence of the transverse flow induced by the free vortices themselves [2]. Then, the wake becomes completely turbulent and three-dimensional over a distance closer and closer to the cylinder as Reynolds increases. Similarly, the turbulent transition point moves upstream towards the separation point with increasing Reynolds numbers.

Except for turbulent effects (dispersion, dissipation...), the flow topology is similar to that of the laminar regime with a vortex street configuration having a stable Strouhal number close to 0.2. One of the first characteristics which can be clearly visualized is that the transverse spacing of the vortex street decreases drastically. Thus, the vortex centers are almost located on the wake centerline. The decrease of the recirculation region, which is also called the formation zone, is easily seen. At $Re \approx 2000$, the length of the recirculation area is almost two diameters. This length decreases with increasing Reynolds number. There are several methods to estimate this length, as summarized by Zdravkovich [1] page 103:
i/ the disappearance of low frequency irregularities
ii/ the crossing of the wake axis by the entrained stream
iii/ the location of maximum streamwise velocity fluctuations in the wake
iv/ the location of minimum mean C_p (pressure coefficient) along the wake axis, which corresponds to the station where the eddies are fully developed.
The resulting length decreases from $2d$, where d is the diameter of the cylinder, at $Re = 2000$ to $1.1d$ at $Re = 14\ 000$. This diminishing is partly due to the small-scale vortices formed at the edge of the recirculation region. When the intensity of the transition waves has become sufficiently energetic, they roll up into small-scale vortices which are convected downstream by the main Kármán vortices, "ridging on their perimeter" [2]. Some of them gather together thereby forming bigger structures, some migrate further downstream and vanish. Then, they contribute to accelerate the transition to turbulence, acting as a kind of catalyst. Another effect of the three-dimensional instabilities of the shear layer vortices seems to be the appearance of streamwise vortices in the wake [16].

Bloor [29] investigated the instability vortices appearing in the free shear layers. By considering the laminar boundary layer thickness and the velocity at the separation point, Bloor showed that the normalized shear layer instability frequency, f_{SL}, scaled

with $Re^{1/2}$. If f_κ denotes the Kármán vortex shedding frequency, then: $\frac{f_S L}{f_\kappa} \propto Re^{1/2}$. Nevertheless, according to Williamson [16], a best fit to all of the studies combined would be proportional to $Re^{0.67}$.

As in the laminar flow regime, a secondary vortex street seems to occur in the far-wake. The primary turbulent vortex street breaks down at a downstream distance approxiamtely equal to $80 - 100$ diameters and is apparently not much dependent on the Reynolds number [2]. Further downstream, a secondary vortex street with organized structures occurs, but at a larger distance from the cylinder than in the laminar regime and with a greater dispersion.

Quite recently, Prasad & Williamson [30] showed that oblique and parallel shedding could be triggered at high Reynolds number ($Re = 5000$) by manipulating the end conditions as in the laminar flow regime. This is really important because the phase of the shedding and the spanwise correlation affect the total integrated unsteady forces on the uniform circular cylinder. As pointed out by Williamson [16], most of the attention in the literature has been given to the case of low aspect ratios, for which the vortices are shed almost in phase across the span. But, "the question of the conditions under which dislocations and cellular shedding may appear at high Reynolds numbers requires further understanding" [16].

3 Linear Shear Flow

When the flow behaviour past tapered circular cylinders at low Reynolds numbers was investigated (see Appendix B and Appendix C), the results obtained and the different flow characteristics observed appeared to be, at least, qualitatively similar to what was reported in the literature on linear shear flows past uniform circular cylinders. This is the reason why it has been found interesting to give a brief description of the main features of the latter configuration. Here, however, the following description is restricted to the laminar flow regime and to the case where the profile of the velocity gradient is located in a streamwise-spanwise plane, as it can be seen in Figure 5. The two sketches (a) and (b) in Figure 5 represent the difference between a nonlinear shear incoming flow and linear shear incoming flow, respectively.

The flow behaviour behind a uniform circular cylinder with linear shear incoming flow is strongly dependent on (at least) three parameters: the Reynolds number, the aspect ratio and the shear parameter β. The aspect ratio is defined as $A_r = l/d$, whereas the shear parameter is defined as $\beta = \frac{d}{u_m}\frac{\partial u}{\partial z}$, where u_m denotes the average free stream velocity. It is not known precisely how many flow parameters influence the behaviour of the wake flow [31].

The first difference between linear shear flow and uniform flow past a uniform circular cylinder is that, with the former, the flow is three-dimensional and not nominally two-dimensional, as expected with the latter. As the free stream approaches the circular cylinder, the shear velocity establishes a spanwise pressure gradient. This induces a secondary flow along the stagnation line from the high-velocity end towards the low-velocity end. On the opposite side of the cylinder, however, the pressure gradient induces a secondary flow towards the high-velocity end [1]. In a streamwise-crosswise plane, the vorticity filaments appear to be distorted by the cylinder, thus two streamwise filaments are emited behind the cylinder (see Figure 15.24(c) in [1]). The streamwise vorticity

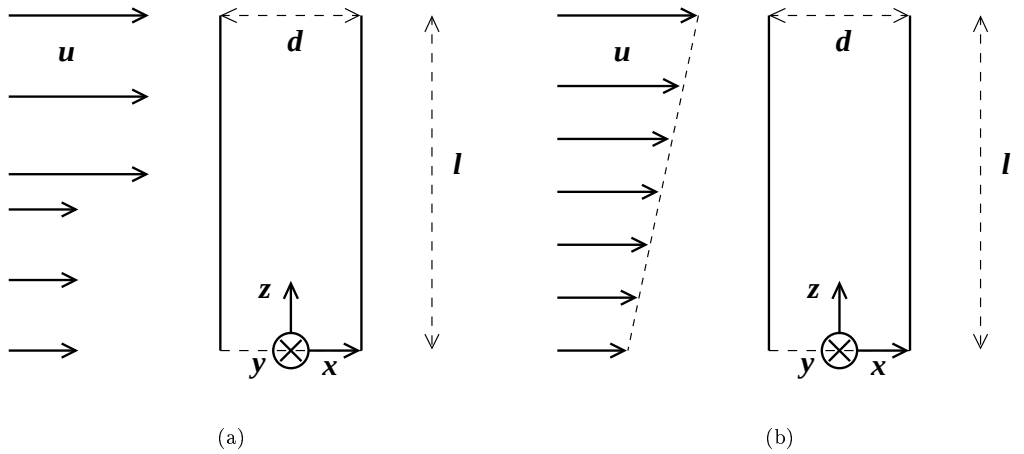

Figure 5: Sketch of two types of shear flow. (a) nonlinear shear flow; (b) linear shear flow.

induces a convective velocity at both sides of the cylinder directed towards the low-velocity region.

Although a cellular pattern has been observed, the vortex shedding phenomenon in the linear shear flow along the span has been found to be different to that of uniform flow. The continuous variation of the free stream velocity does not lead to a continuous variation in shedding frequency [1]). The span of the cylinder can be divided into several cells, each of them being characterized by one shedding frequency. The length of the cells observed experimentally (see the review by Griffin [32]) as well as these computed by Mukhopadhyay et al. [31] vary between three and seven diameters. Within each cell, the Strouhal number based on the mean velocity is constant, while the Strouhal number based on the local velocity varies linearly, with sudden "jumps" across the cell boundaries [31]. Mukhopadhyay et al. [31] noticed that due to the complex fluid dynamic interactions that are occuring in the near wake, the Strouhal number for linear shear flow was lower than the Strouhal number for uniform flow. This seemed to be a result of continuous spanwise energy redistribution. Based on the centreline free stream velocity, the Strouhal number ranged roughly $0.13 - 0.20$.

Another characteristic which has been described both experimentally [33] and numerically [31] is that the cell boundaries moved in time along the span and were not fixed. Moreover, it has been shown that the end conditions had a strong influence on the cell pattern and the wake flow dynamic. Mair & Stansby [33] noticed that the effect of the end conditions were much more pronounced when a cylinder with a small aspect ratio was used than with cylinder with large A_r. With $A_r < 20$, no cells could be determined between the two end cells, the whole span was affected by the end conditions. However, Mair & Stansby showed that it was possible to get cells by using end plates placed at the extremities of the cylinder. Moreover, large end plates proved to have a stabilizing effect on the cell pattern. Mukhopadhyay et al. performed computations with and without end plates at the extremities of the cylinder span. The end wall boundary layers, due to

the end plates, did not produce much distortion in the vorticity results compared to the case without end plates. At last, vortex dislocations were observed in both cases near the high-velocity end of the circular cylinder and there were convected downstream.

Part IV
Results

The results obtained from the simulations done for this project have been reported in several papers which are presented herein in the Appendices. Nevertheless, for the sake of completion, it has been decided to provide some details and "extra" results which do not appear in these papers.

1 Laminar Flow

Three different kind of simulations have been performed at low Reynolds numbers: two-dimensional numerical simulations of flow past a circular cylinder (see Appendix B), and three-dimensional numerical simulations of flow past a stepped circular cylinder (see Appendix A) and past tapered circular cylinders (see Appendix B and Appendix C).

1.1 Two-Dimensional Simulations

The two-dimensional numerical simulations allowed us to perform several tests on different parameters at a relatively low cost in cpu-time. The Reynolds number was fixed at 200 for which comparisons with experimental and other numerical results were possible. The aim was to determine a set of parameters giving the best ratio accuracy/cpu-time consumption. These parameters were the time step and the convergence criterion for the Newton iteration (previously described in Part II). Moreover, the effect of the mesh size on the choice of parameters have been investigated too. The complete results for all the tests performed, from which Table 1, Table 2 and Figure 1 in Appendix B are extracted, are reported here.

Besides the results of our simulations given in Table 3, experimental (Roshko), theoretical (Williamson) and other numerical (Multigrid, Belov et al., Braza et al.) results are reported. They are described in Appendix B Section 3.

Firstly, the effect of the mesh size has been investigated. The set of parameters used was: 10^{-2} for the convergence criterion and 0.1 for the dimensionless time step $\Delta t \frac{U}{d}$. The convergence criterion for the Newton iteration is defined as the ratio of the Root Mean Square (RMS) of the residual at the given iteration to the RMS of the residual at the first iteration. When the total cpu-time consumption per vortex shedding period per grid point is considered, the 200×200 mesh appears to be the best compromise. The 100×100 and 200×200 meshes had similar ratio cpu-time/grid point: 0.216 and 0.243, respectively, whereas the 400×400 had a ratio of 0.305. This is because more Newton iterations are needed for a given convergence criterion on the finer mesh. Thus, the 200×200 mesh gave the best accuracy relatively to a low cpu-time consumption. Secondly, once the mesh size had been chosen, the effect of different sets of parameters

Table 3: Comparison of drag coefficient (C_d), lift coefficient (C_l) and Strouhal number (St) for two-dimensional vortex shedding at $Re = 200$. cc: convergence criterion, ts: time step.

Reference	C_d	C_l	St
100×100 ($cc = 10^{-2}$, $ts = 0.1$)	1.395	$\pm$ 0.661	0.1926
200×200 ($cc = 10^{-4}$, $ts = 0.05$)	1.413	$\pm$ 0.686	0.1963
200×200 ($cc = 10^{-4}$, $ts = 0.1$)	1.411	$\pm$ 0.684	0.1952
200×200 ($cc = 10^{-4}$, $ts = 0.2$)	1.405	$\pm$ 0.659	0.1917
200×200 ($cc = 10^{-3}$, $ts = 0.05$)	1.413	$\pm$ 0.686	0.1963
200×200 ($\mathbf{cc = 10^{-3}}$, $\mathbf{ts = 0.1}$)	**1.411**	**$\pm$ 0.684**	**0.1952**
200×200 ($cc = 10^{-3}$, $ts = 0.2$)	1.405	$\pm$ 0.659	0.1916
200×200 ($cc = 10^{-2}$, $ts = 0.05$)	1.413	$\pm$ 0.684	0.1964
200×200 ($cc = 10^{-2}$, $ts = 0.1$)	1.409	$\pm$ 0.678	0.1933
200×200 ($cc = 10^{-2}$, $ts = 0.2$)	1.404	$\pm$ 0.657	0.1909
400×400 ($cc = 10^{-2}$, $ts = 0.1$)	1.410	$\pm$ 0.687	0.1956
Multigrid	1.2[a]	$\pm$ 0.68[a]	0.195
Belov et al.	1.232	$\pm$ 0.64	0.193
Braza et al.	1.3	$\pm$ 0.775	0.20
Williamson	-	-	0.197
Roshko	-	-	$0.18 - 0.20$

[a] Pressure forces only

on the ratio accuracy/cpu-time consumption was investigated. The best compromise was found to be for a convergence criterion equal to 10^{-3} and a time step equal to 0.1. This can be seen in Table 3 and Table 4, herein, and in Figure 1 Appendix B where results for Strouhal number are compared. Increasing the accuracy further by any of the means considered, only marginally changes the results for C_d, C_l and St.

1.2 Three-Dimensional Simulation

The results of the three-dimensional numerical simulations we performed at low Reynolds numbers have been reported in three papers (see Appendixes A through C). Appendix A presents the results obtained for the simulation of flow past a stepped circular cylinder, whereas the flow past tapered circular cylinders is concerned in Appendixes B and C.

1.2.1 Stepped Circular Cylinder

As mentioned in Part I, the aim was to reproduce the experimental investigations done by Lewis & Gharib [5] for a uniform flow past stepped circular cylinders. Lewis & Gharib performed an extensive series of experiments on 5 different stepped circular cylinders. Each cylinder being characterized by its diameter ratio $r = d_L/d_S$ (see Figure 1(a)). The diameter ratio can also be expressed with the Reynolds numbers based on the small and large diameters, such that: $r = Re_L/Re_S$.

In the experiments, two distinct types of wake behaviour, called the direct and indirect modes of interaction by Lewis & Gharib, were found. Because a stepped cylinder has two

Table 4: Comparison of total cpu-time consumption per period of two-dimensional vortex shedding at $Re = 200$. cc: convergence criterion, ts: time step.

Reference	Number of Processors	Total cpu-time[a] per period
100×100 ($cc = 10^{-2}$, $ts = 0.1$)	8	36
200×200 ($cc = 10^{-4}$, $ts = 0.05$)	16	557
200×200 ($cc = 10^{-4}$, $ts = 0.1$)	16	335
200×200 ($cc = 10^{-4}$, $ts = 0.2$)	16	215
200×200 ($cc = 10^{-3}$, $ts = 0.05$)	8	392
200×200 ($\mathbf{cc = 10^{-3}}$, $\mathbf{ts = 0.1}$)	**8**	**220**
200×200 ($cc = 10^{-3}$, $ts = 0.2$)	8	133
200×200 ($cc = 10^{-2}$, $ts = 0.05$)	8	261
200×200 ($cc = 10^{-2}$, $ts = 0.1$)	8	162
200×200 ($cc = 10^{-2}$, $ts = 0.2$)	8	87
400×400 ($cc = 10^{-2}$, $ts = 0.1$)	32	781

[a] in minutes

different diameters, the vortices of the small diameter part will be shedded at a different frequency than those of the large diameter part. Hence, an interaction region between the wakes of the two parts of the cylinder will occur at the interface. The interface zone, which originates from the step, is defined by the plane where the vortex lines are interrupted [5].

The occurence of the direct and indirect modes seemed to be a function of the diameter ratio and the Reynolds number. Based on the diameter ratio, Lewis & Gharib classified the interaction region into three categories:

$r < 1.25$: direct mode dominates,

$1.25 < r < 1.55$: transitional (mode is a function of Re),

$r > 1.55$: indirect mode dominates.

The indirect mode is characterized by three distinct vortex-shedding frequencies, f_S and f_L for the small and large part of the cylinder and a third one, noted f_3 always inferior to f_S and f_L. The region where the third frequency occurs, close to the interface in the large-diameter wake, is called the modulated zone. This region is said to act as a buffer between the two wake frequencies f_S and f_L [5]. At the interface zone, the vortices link along a line almost orthogonal to the cylinder axis. Another main feature of the indirect mode is the occurence of an inclined interface at a frequency $f = f_L - f_3$ which extends spanwise across the modulated zone on a significant angle [5].

The direct mode is characterized by the two distinct vortex-shedding frequencies f_S and f_L. They interact directly in the interaction region, said to be a zone of quasiperiodic frequency interaction. A feature of the direct mode is the vortex linkage at the interface zone. "The vortices connect across the interface zone when they are in phase (or nearly so). As they become more out of phase, the vortices form linkages to one another on the same side of the interface. As a result, a hole is formed in the vortex pattern, representing an absence of vortex tubes" [5]. Moreover, there are more vortices shedded on the small part of the cylinder than on the other one, leading to some "extra" vortices.

An "extra" vortex will be not linked across the interface to another of the large diameter part. Hence, this extra vortex will form a "half-loop" [5]. The linkage phenomenon takes place at $\pm 5 d_L$ in the spanwise direction from the interface.

Another distinctive characteristic of the direct mode is the appearance of angled shedding throughout the wake, and especially behind the the large-diameter part. Lewis & Gharib [5] noticed that the shedding angles in the small-diameter wake remained low whereas in the large-diameter wake they were steep. However, both of them remained constant and fixed for each of the direct mode cases they studied. In fact, Lewis & Gharib [5] noticed that the "direct mode of interaction only occurred for the range of Reynolds number for which the d_L wake shedding angle was steep and fixed". The global range of Reynolds number was: $70 < Re < 134$ for cylinders with diameter ratio equal to 1.34 and 1.53. The indirect mode occurring below and above this Reynolds number range. Figure 19 in [5], depicts the mode appearance as a function of Reynolds number and diameter ratio.

The results for the case undertaken compared quite well with the experimental study made by Lewis & Gharib [5] (see Appendix A). Qualitatively, all the different characteristics of the direct mode of interaction were reproduced: the shedding angle of the vortices (almost parallel to the cylinder axis in the small-diameter wake and steep in the large-diameter one), the hole-shaped pattern and the half-loop phenomenon. Quantitatively, however, some small discrepancies have been found. They are assumed to be due to the difference in boundary conditions between the experimental works and the numerical study.

1.2.2 Tapered Circular Cylinders

The numerical investigations of flow behaviour behind tapered circular cylinders at low Reynolds numbers performed in this project, have been reported in the papers placed in Appendix B and Appendix C.

The numerical simulations aimed at reproducing the experimental work done by Piccirillo & Van Atta [6]. They used four different tapered circular cylinders, each of them characterized by their taper ratio $R_T = l/(d_L - d_S)$. Figure 1(b) depicts a typical tapered circular cylinder.

Piccirillo & Van Atta [6] noticed that the more tapered the cylinder was (which means small R_T), the less ordered the cell structure and the wake flow were. At first, we were interested in the wake flow differences between tapered circular cylinder and uniform circular cylinder. This is the reason why the cylinder with $R_T = 100 : 1$ had been chosen. Indeed, the slight difference in geometry induced rather different wake phenomena. Moreover, the fact that the cylinder with $R_T = 100 : 1$ was the more "ordered" cylinder rendered the comparisons between numerical simulation and experimental results easier. Then, in order to provide more detailed comparisons between the two studies, a second tapered circular cylinder was chosen. It appeared that the cylinder for which the most results were available, was the tapered circular cylinder with $R_T = 75 : 1$. With this cylinder, we have been able to reproduce all the main characteristics described by Piccirillo & Van Atta. Especially the vortex splitting occuring at the narrow end of the tapered circular cylinder of our Case B.

When the results from Appendix B and Appendix C are compared for our Case A, a difference in the number of cells can be seen. In Appendix B, we stated that three

shedding cells were found, the same as in the experiments, while in Appendix C, we described five shedding cells, the same as in the numerical simulation performed by Jespersen & Levit [34] ten years earlier. In fact, it appeared that we did not run the simulation sufficiently long enough to get a fully established periodic wake when we reported our results in Appendix B. By looking at animations of the time evolution of the wake flow, we realized that new shedding cells were created. At last, the cell structure was made up of five cells.

Figure 6 in Appendix C represents the Strouhal-Reynolds relationships from our simulations compared with other results. It would have been possible to plot our results differently. If for each shedding cell, the Strouhal numbers had been calculated with the mean diameter of the shedding cell, then the curves would have been a succession of plateau because the vortex shedding frequency is constant within each cell. Moreover, to exactly compare our results with the experiments done by Piccirillo & Van Atta [6], we should have plotted only one Strouhal number value per shedding cell, as they did. Instead of these methods, we decided to calculate the Strouhal numbers based on the local diameter thereby plotting local Strouhal number versus local Reynolds number. This had the advantage to allow us to see the effect of a vortex splitting on the vortex shedding frequency. This would have been difficult or impossible to see by using the two other methods. Consequently, we did not loose this important information.

As mentioned in Appendix C, most of the vortex shedding phenomena occuring behind tapered circular cylinders were similar to these described by Mukhopadhyay et al. [31] for linear shear flow past a uniform circular cylinder. In a recent numerical investigation, Willden & Graham [35] performed simulations of linear shear flow past uniform circular cylinders at low Reynolds numbers, using a quasi three-dimensional method. This method means that multiple two-dimensional computational planes are placed along the cylinder span. They performed two kind of simulations, with and without vibrating cylinders in a range of Reynolds number similar to Mukhopadhyay et al. [31]. For the case of a stationary cylinder, the spanwise evolution of the Strouhal number seems to be in good agreement, though they are slightly overestimated compared to [31]. Figure 7 in [35] presents the time evolution of the lift coefficient, C_l, acting on the cylinder. Unfortunately, this cannot be compared with other results. Nevertheless, it seems, due to the bending of the lines on the top of the figure, that a vortex splitting occur near $t = 260$. Surprizingly, the global pattern of this figure looks more like what we obtained when we performed simulation of flow past a stepped circular cylinder. Although absolutely no conclusions can be drawn from this observation, it contributes to the question whether or not linear shear flow past uniform circular cylinder and uniform flow past tapered circular cylinder can be compared. This requires further investigations to be answered and understood.

2 Turbulent Flow

Large-eddy simulation of turbulent flow have been performed for two uniform circular cylinders. The results are presented in Appendix D. The objective was to prove that our code, CBJ, was able to solve turbulent flow by means of large-eddy simulation. Therefore, simulations for two different uniform circular cylinders were performed as test cases. Uniform circular cylinder were chosen because of the large amount of experimental and numerical results available in the literature. Moreover, a brief description of the turbulent

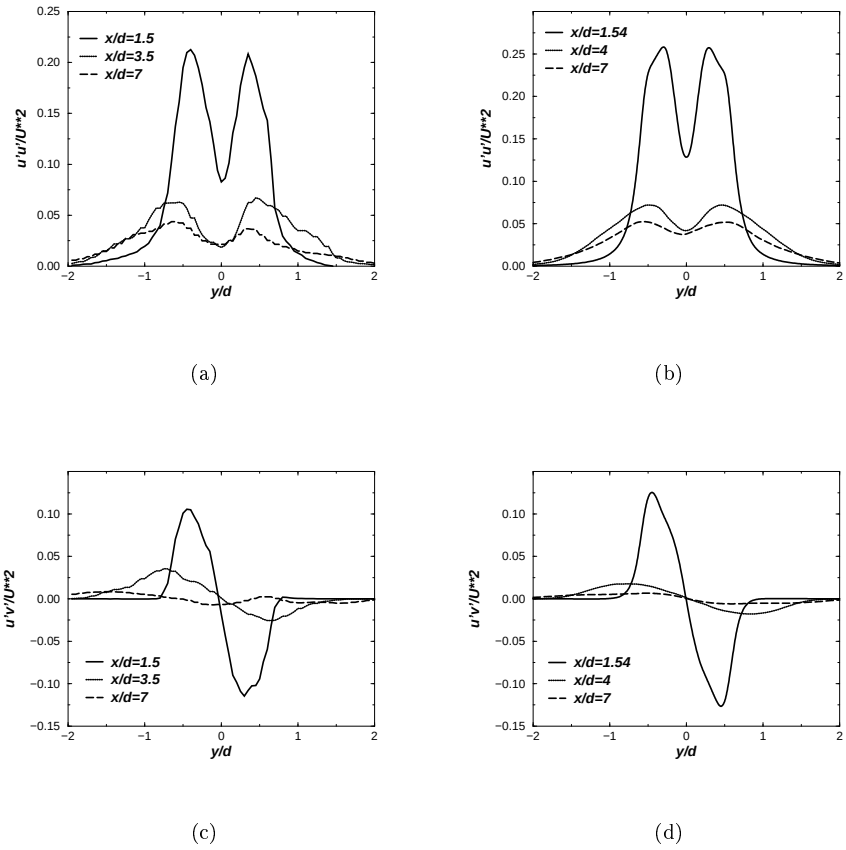

Figure 6: Statistics in the near wake region. Evolution in the streamwise direction of: variance of the streamwise velocity component, (a) LES and (b) DNS; shear stress, (c) LES and (d) DNS

flow behaviour past a tapered circular cylinder at high Reynolds number expected to be numerically obtained is also provided.

2.1 Uniform Circular Cylinder

The first test case, called Case 1 in Appendix D, had a quite coarse mesh. This enabled us to investigate different parameters (time step, time differenciation) at a somewhat low cost in cpu-time.

With Case 2, care was taken to have good resolution close to the cylinder. Here, the first grid point was almost equal to the Kolmogorov length scale: $0.2 \cdot 10^{-3}d$ at $Re = 3900$. At this Reynolds number the transition to turbulence takes place in the free shear layers (see Part III), then on the cylinder the boundary layer remains laminar. A rough estimate of the boundary layer size δ, is given by [11, 1]: $\delta = 5/\sqrt{Re}$. Thus, with

$Re = 3900$, $\delta \approx 0.08$. Here, with our mesh, there are 33 grid points across the boundary layer from the cylinder to the free stream. Five diameters downstream from the cylinder, the size of the cells in planes orthogonal to the cylinder axis was 3.5 times larger. At the far field boundary, 20 diameters downstream, the size of the cells in the same planes was 200 times the Kolmogorov length scale. In the spanwise direction, the size of the cells were 37.5 times bigger than the Kolmogorov scale. Consequently, as shown in Table 1 Appendix D, the total cpu-time consumption for Case 2 was 10 times bigger than for Case 1.

The results for Case 2 compared favourably with both experimental and DNS results. However, besides the results presented in Appendix D, it has been found interesting to provide a comparison, between our data and the DNS done by Tremblay et al. [8], of the evolution in the streamwise direction of: i/ the variance of the streamwise velocity component (Figure 6(a) and Figure 6(b)); ii/ the shear stress profiles (Figure 6(c) and Figure 6(d)). The results are in quite good agreement, the different profiles are similar and the behaviour identical. Nevertheless, the LES results underestimate slightly the DNS results for the variance of the streamwise velocity component. It must be noticed that the shear stress at $x/d = 7$ in our LES results begins to be no more symmetric relatively to the abscissa axis. This means that our grid is not fine enough from $x/d = 7$ to $x/d = \infty$ to resolve the small structures. However, both LES and DNS results in Figure 6 are 70 percent lower at $x/d = 3.5 - 4$ than those at $x/d = 1.5$.

As mentioned in Appendix D, periodic boundary conditions in the spanwise direction have been used to mimic infinitely long cylinders. This can be a source of debate. In Part III Section 2 we reported the recent work of Prasad & Williamson [30], namely that oblique shedding mode could occur at high Reynolds numbers for cylinders with large aspect ratios. With periodic boundary conditions it is assumed that the vortices are shedded in phase along the span, thus only parallel shedding is simulated. Consequently, when one wants to reproduce numerically the turbulent flow past a uniform infinitely long (large aspect ratio) circular cylinder, periodic boundary conditions should not be used. But, because the occurence of oblique vortex shedding mode at high Reynolds numbers is still not well understood, the question of whether or not periodic boundary conditions can be used remains open.

2.2 Tapered Circular Cylinder

The aim of the large-eddy simulation of flow past the tapered circular cylinder considered here is to reproduce one of the experiment done by Hsiao & Chiang in 1998 [9]. The choice of this geometrical configuration (detailed in Table 2) is justified by its use in several studies in the laminar flow regime [6, 34] as well as in the turbulent flow regime [9]. Moreover, the shear parameter β used by Mukhopadhyay et al. [31] in their study of linear shear flow past uniform circular cylinders, was $\beta = 0.02$ which is equivalent to a taper ratio R_T of $50 : 1$, as mentioned in Appendix C. Hence, this geometry seems to provide the possibility to compare results from a broad range of different works.

The main characteristics of the turbulent flow behind a tapered circular cylinder at high Reynolds numbers are similar to the characteristics observed in the laminar flow regime. The vortices are shedded with an angle relative to the cylinder axis and the span of the cylinder can be divided into several shedding cells, each cell having its own constant vortex shedding frequency. The vortex splitting phenomenon, as previously

described (see Part IV Section 1.2.2 and Appendix C), can also be observed. The vortex shedding frequency is higher at the narrow end of the cylinder than at the wide end.

One of the main differences between the laminar flow and the turbulent flow past a tapered circular cylinder is that in the case of turbulent flow, the whole span of the cylinder is always shedding vortices [9]. Moreover, for the case considered here, only two vortex shedding cells with identical size are expected to occur. Their size being equal to half the cylinder span.

The expected Strouhal number would be in range of $0.18 < St < 0.20$. According to Hsiao & Chiang [9], at a given taper ratio, the range of Strouhal number increases with the Reynolds number (for $Re = 1.4 \times 10^4$ the range is $0.20 < St < 0.22$). The average Strouhal number is then higher than the average observed by Piccirillo & van Atta in the laminar flow regime. Compared to the range of Strouhal numbers obtained for the case of the turbulent flow past a uniform circular cylinder, the Strouhal number values for the flow past a tapered circular cylinder are somewhat lower. The same is observed in the laminar flow regime (see Appendix C).

Part V
Concluding Remarks

A computational study of vortex shedding behind different types of bluff bodies has been done. By using the Concurrent Block Jacobi solver, it has been possible to perform three-dimensional numerical simulations of flow behind stepped and tapered circular cylinders in laminar flow regime and behind uniform circular cylinders in turbulent flow regime. The main characteristics of these flows which have been reported in the literature for experimental, theoretical and numerical investigations, were successfully reproduced. Moreover, numerical simulations yield much more detailed information than experiments as all the data is known at every grid point for all time steps. This can contribute to a better understanding of the vortex shedding phenomenon.

However, this study clearly shows that it is still not possible today to reproduce numerically all the types of flow encountered in daily life. Despite the great improvement of computer capabilities, we are still limited by the memory usage and the storage capacity required by the simulations. These limitations have been encountered in this study, especially when large-eddy simulation of flows past circular cylinders were undertaken.

Although the present work has shown many of the aspects of the vortex shedding phenomenon and wake flow three-dimensionalities occuring behind circular cylinders, much has still to be down before one will understand perfectly all the details of such flows. Hence, future investigations should concentrate on: for the laminar flow regime, the completion of the stepped circular cylinder study in order to reproduce the indirect mode of interaction and to explore the areas in the "diameter ratio-Reynolds number" diagram of Lewis & Gharib [5], for which the mode of interaction is unknown. It would also be interesting to perform other numerical simulations of flow past tapered circular cylinders in order to precisely compare the results with those of linear shear flow past uniform circular cylinders. For the turbulent flow regime, a thorough investigation of the vortex shedding behind tapered circular cylinders should be done, this case being of

great practical interest in engineering. Moreover, it would be interesting to implement the CBJ solver with a subgrid dynamic model, known to usually give more accurate results.

References

[1] M. M. Zdravkovich. *Flow around Circular Cylinders. Vol.1: Fundamentals.* Oxford University Press, 1997.

[2] M. Coutanceau and J.-R. Defaye. Circular cylinder wake configurations: a flow visualization survey. *Appl. Mech. Rev.*, 44:255–305, 1991.

[3] M. Lesieur and O. Métais. New trends in large-eddy simulations of turbulence. *Annu. Rev. Fluid. Mech.*, 28:45–82, 1996.

[4] M. Breuer. Large eddy simulation of the subcritical flow past a circular cylinder: numerical and modeling aspects. *Int. J. Numer. Meth. Fluids*, 28:1281–1302, 1998.

[5] C. G. Lewis and M. Gharib. An exploration of the wake three dimensionalities caused by a local discontinuity in cylinder diameter. *Phys. Fluids*, A 4:104–117, 1992.

[6] P. S. Piccirillo and C. W. Van Atta. An experimental study of vortex shedding behind linearly tapered cylinders at low Reynolds number. *J. Fluid Mech.*, 246:163–195, 1993.

[7] C. Norberg. An experimental investigation of the flow around a circular cylinder: influence of aspect ratio. *J. Fluid Mech.*, 258:287–316, 1994.

[8] F. Tremblay, M. Manhart, and R. Friedrich. DNS of flow around a circular cylinder at a subcritical Reynolds number with cartesian grids. In C. Dopazo et al., editors, *Advances in Turbulence VIII*, pages 659–662, Barcelona Spain, June 2000. CIMNE.

[9] F.-B. Hsiao and C.-H. Chiang. Experimental study of cellular shedding vortices behind a tapered circular cylinder. *Exp. Therm. Fluid Sci.*, 17:179–188, 1998.

[10] C. B. Jenssen. *The development and implementation of an implicit multi block Navier-Stokes solver.* PhD thesis, Dept. of Mechanical Engineering, Norwegian Inst. of Technology, Trondheim, Norway, 1992.

[11] H. Schlichting. *Boundary-layer theory.* McGraw-Hill, 7^{th} edition, 1979.

[12] C. B. Jenssen and P. Å. Weinerfelt. Parallel implicit time-accurate Navier-Stokes computations using coarse grid correction. *AIAA J.*, 36:946–951, 1998.

[13] C. Hirsch. *Numerical computation of internal and external flows*, volume 2. John Wiley & Sons, 1990.

[14] C. Hirsch. *Numerical computation of internal and external flows*, volume 1. John Wiley & Sons, 1988.

[15] C. B. Jenssen and P. Å. Weinerfelt. Coarse grid correction scheme for implicit multiblock Euler calculations. *AIAA J.*, 33:1816–1821, 1995.

[16] C. H. K. Williamson. Vortex dynamics in the cylinder wake. *Annu. Rev. Fluid Mech.*, 28:477–539, 1996.

[17] M. Provansal, C. Mathis, and L. Boyer. Bénard-von Kármán instability: transient and forced regimes. *J. Fluid Mech.*, 182:1–22, 1987.

[18] C. H. K. Williamson. Defining a universal and continuous Strouhal-Reynolds number relationship for the laminar vortex shedding of a circular cylinder. *Phys. Fluids*, 31:2742–2744, 1988.

[19] C. H. K. Williamson. Oblique and parallel modes of vortex shedding in the wake of a circular cylinder at low Reynolds numbers. *J. Fluid Mech.*, 206:579–627, 1989.

[20] D. J. Tritton. Experiments on the flow past a circular cylinder at low Reynolds numbers. *J. Fluid Mech.*, 6:547–567, 1959.

[21] D. J. Tritton. A note on vortex streets behind circular cylinders at low Reynolds numbers. *J. Fluid Mech.*, 45:203–208, 1971.

[22] M. Gaster. Vortex shedding from slender cones at low Reynolds numbers. *J. Fluid Mech.*, 38:565–576, 1969.

[23] M. Gaster. Vortex shedding from circular cylinders at low Reynolds numbers. *J. Fluid Mech.*, 46:749–756, 1971.

[24] C. H. K. Williamson and G. L. Brown. A series in $1/\sqrt{Re}$ to represent the Strouhal-Reynolds number relationship of the cylinder wake. *J. Fluids Struct.*, 12:1073–1085, 1998.

[25] C. H. K. Williamson. The existence of two stages in the transition to three-dimensionality of a cylinder wake. *Phys. Fluids*, 31:3165–3168, 1988.

[26] H. Eisenlohr and H. Eckelmann. Vortex splitting and its consequences in the vortex street wake of cylinders at low Reynolds number. *Phys. Fluids*, A 1:189–192, 1989.

[27] T. Leweke, M. Provansal, G. D. Miller, and C. H. K. Williamson. Cell formation in cylinder wakes at low Reynolds numbers. *Phys. Rev. Letters*, 78-7:1259–1262, 1997.

[28] P. Albarède and A. Monkewitz. A model for the formation of oblique shedding and 'chevron' patterns in cylinder wakes. *Phys. Fluids*, A 4:744–756, 1992.

[29] M. S. Bloor. The transition to turbulence in the wake of a circular cylinder. *J. Fluid Mech.*, 19:290–304, 1964.

[30] A. Prasad and C. H. K. Williamson. Three-dimensional effects in turbulent bluff-body wakes. *J. Fluid Mech.*, 343:235–265, 1997.

[31] A. Mukhopadhyay, P. Venugopal, and S. P. Vanka. Numerical study of vortex shedding from a circular cylinder in linear shear flow. *J. Fluids Engng (Trans. ASME)*, 121:460–468, 1999.

[32] O. M. Griffin. Vortex shedding from bluff bodies in a shear flow: a review. *J. Fluids Engng (Trans. ASME)*, 107:298–306, 1985.

[33] W. A. Mair and P. K. Stansby. Vortex wakes of bluff cylinders in shear flow. *SIAM J. Appl. Math.*, 28:519–540, 1975.

[34] D. C. Jespersen and C. Levit. Numerical simulation of flow past a tapered cylinder. *AIAA paper*, 91–0751, 1991.

[35] R. H. J. Willden and J. M. R. Graham. Numerical predictionof VIV on long flexible circular cylinders. *J. Fluids Struct.*, 15:659–669, 2001.

Appendices

Appendix A

B. Vallès, H. I. Andersson and C. B. Jenssen. Direct-mode interactions in the wake behind a stepped cylinder. Submited for publication as a brief communication, 2001.

Appendix B

B. Vallès, H. I. Andersson and C. B. Jenssen. Three-dimensional numerical simulation of laminar flow past a tapered circular cylinder. In C. B. Jenssen et al, editors, *Parallel Computational Fluid Dynamics- Trends and Applications*, pages 581–588, Elsevier Science B. V., 2001.

Appendix C

B. Vallès, C. B. Jenssen and H. I. Andersson. Oblique vortex shedding behind tapered cylinders. *J. Fluids Structures*, (accepted) 2001.

Appendix D

B. Vallès, H. I. Andersson and C. B. Jenssen. Large-eddy simulation of turbulent flow past straight and tapered circular cylinders. Accepted for publication in *Direct and Large-Eddy Simulation - IV* conference proceedings, Enschede, The Netherlands, July 18-20 2001.

Appendix A

Appendix A is not included due to copyright restrictions.

Appendix B

Appendix B is not included due to copyright restrictions.

Appendix C

Oblique Vortex Shedding behind Tapered Cylinders*

Brice Vallès[1] Helge I. Andersson[1] Carl B. Jenssen[2]

[1] Department of Applied Mechanics, Thermodynamics and Fluid Dynamics
Norwegian University of Science and Technology, N-7491 Trondheim, Norway
brice.valles@mtf.ntnu.no helge.i.andersson@mtf.ntnu.no

[2] Statoil R & D Centre, N-7005 Trondheim, Norway. CABJ@statoil.com

July 31, 2001

Abstract

The vortex shedding in the wake behind linearly tapered circular cylinders has been considered for the two taper ratios 75 : 1 and 100 : 1. The Reynolds number based on the velocity of the incoming flow and the largest diameter was in the range from 130 to 180. The low Reynolds number assured that laminar flow prevailed in the entire flow field. The full unsteady three-dimensional Navier-Stokes equations were solved numerically with the view to explore the rather complex vortex shedding phenomena caused by the variation of the natural shedding frequency along the span of the cylinder. The accurate computer simulations showed that this variation gave rise to discrete shedding cells, each with its own characteristic frequency and inclined with respect to the axis of the cylinder. Flow visualizations revealed that vortex dislocation and splitting took place in the numerically simulated flow fields. The computer simulations compared surprisingly well with the extensive laboratory experiments reported by Piccirillo & Van Atta (J. Fluid Mech. **246**, pp. 163-195, 1993) under a range of comparable conditions and enabled detailed analyses of other flow variables (notably pressure and vorticity) than those readily accessible in a physical experiment. However, distinct differences in the vortex dynamics are observed in some of the cases.

1 Introduction

The potentially severe consequences of vortex shedding behind bluff bodies was a completely unknown phenomenon among civil engineers until the collapse of Tacoma bridge some 50 years ago. Today, the vortex dynamics in wakes behind geometrically simple objects are quite well understood as long as the shedding is nominally 2-D; see the excellent review by Williamson (1996). 3-D vortex shedding is by far more complex from a physical point of view and therefore relatively less understood. Three-dimensional wake phenomena may for example occur behind circular cylinders if U/D varies along the span of the cylinder, i.e. if either the cylinder diameter D or the incoming velocity U (or both) changes. A geometrically simple configuration, and yet of great practical relevance (e.g. chimneys and oil-platform legs), is the uniform flow past a linearly tapered circular cylinder, of which a slender cone represents a special case. Following the pioneering experimental studies by Gaster (1969, 1971), in-depth laboratory investigations of vortex shedding behind tapered cylinders were performed by Piccirillo & Van Atta (1993), and Papangelou (1992) for the special case of cones, and more recently by Hsiao & Chiang (1998).

Until recently, the majority of investigations of 3-D vortex shedding were performed in the laboratory. Computer simulations, which require accurate solutions of the time-dependent three-dimensional Navier-Stokes equations, have only become feasible in the last decade, e.g. Jespersen & Levit (1991). The

*This paper is based on an oral presentation at the IUTAM Symposium on Bluff Body Wakes and Vortex-Induced Vibrations held in Carry-le-Rouet outside Marseille, France, June 13-16, 2000.

objective of the present study is to perform detailed computer simulations of the three-dimensional laminar vortex shedding behind a linearly tapered cylinder with a two-fold aim: i) to demonstrate how closely the experimental findings of Piccirillo & Van Atta (1993) can be reproduced numerically; and ii) to explore the simulated flow fields with the view to provide details of the complex shedding pattern not readily available in a laboratory experiment. First, however, a brief summary of the most striking vortex shedding phenomena is provided.

2 Vortex Shedding Phenomena

The vortex shedding behind a straight circular cylinder in a uniform incoming flow is a classical example of naturally occuring unsteadiness in fluid dynamics. Following Roshko in 1954, numerous authors have contributed both experimentally, theoretically and numerically to the understanding of intricate and fascinating phenomena such as vortex shedding, vortex splitting, oblique versus parallel shedding, and occurence of flow instabilities (Mode A and Mode B) in the transition-to-turbulence process; see Williamson (1996) for details. For example, a subject of controversy has been the origin of discontinuities in the Strouhal-Reynolds number relationship in the laminar shedding regime, Gaster (1969, 1971) and Tritton (1959, 1971). Williamson (1988) showed that in the parallel shedding regime, the Strouhal-Reynolds number curve was completely continuous. Moreover, the experimental oblique-shedding data closely collapsed onto the parallel-shedding curve defining a universal Strouhal-Reynolds number curve:

$$St = \frac{A}{Re} + B + C \cdot Re \tag{1}$$

where $A = -3.3265$, $B = 0.1816$ and $C = 1.600 \times 10^{-4}$, and the Reynolds number is defined as: $Re = U.D/\nu$, with ν the kinematic viscosity of the fluid. Similarly the Strouhal number, which is a dimensionless frequency parameter, can be defined as: $St = f.D/U$, where f denotes the vortex shedding frequency. Williamson & Brown (1998) showed that a more accurate $St - Re$ relationship could be given by:

$$St = A + \frac{B}{\sqrt{Re}} + \frac{C}{Re} \tag{2}$$

where $A = 0.2850$, $B = -1.3897$ and $C = 1.8061$. According to Williamson & Brown (1998), equation (2) with this set of coefficients is "distinctly more accurate than existing traditional fits".

Next, in order to investigate a somewhat more complex problem, two variants can be studied: a change in incoming flow (even if the uniformity assumption can often be made, in reality this never happens) or a change in geometry (for industrial applications). The former configuration consists of an incoming linear shear flow past a uniform circular cylinder; linear shear flow meaning that the velocity u of the incoming stream varies linearly along the z-axis which is the cylinder axis (see Figure 1(a)). The latter case is that of a uniform incoming flow (U) past a tapered circular cylinder; tapered meaning a constant change in diameter d all along the spanwise (see Figure 1(b)). The former is characterized by a shear parameter: $\beta = (D/u_m)(\partial u/\partial z)$, where D is the diameter of the circular cylinder and u_m denotes the average free stream velocity. The latter is characterized by the taper ratio: $R_T = l/(d_2 - d_1)$, where l is the length of the cylinder and d_2 and d_1 denote the diameters of the wide and narrow ends of the cylinder, respectively. The two flow configurations depicted in Figure 1 may at first sight appear as fundamentally different. However, the observed vortex shedding phenomena turn out to be quite similar (see the review on vortex shedding from bluff bodies in shear flow by Griffin (1985)). Indeed, by assuming that the same fluid is considered in both cases and that $u_m = U$, the relation $\beta = 1/R_T$ is easily shown, thereby justifying at least qualitative comparisons. This suggest the alternative definition $(d_2 - d_1)/l$ of the taper ratio.

Nevertheless, an important distinction between the linear shear flow and the uniform flow past a tapered cylinder should be pointed out. In the former case, the local stagnation pressure varies essentially proportionally to u^2, as does the base pressure along the lee side; see e.g. Zdravkovich (1997). The

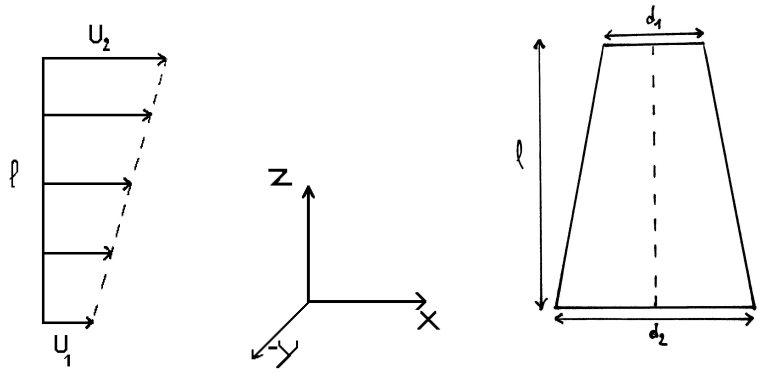

(a) (b)

Figure 1: Sketch of: (a) linear shear flow, (b) tapered cylinder

associated pressure gradients along the span give rise to a pressure-driven secondary flow along the stagnation line from the high-velocity end towards the low-velocity end, and an oppositely directed flow along the lee side of the cylinder. In the tapered case, on the other hand, the stagnation pressure and the base pressure are practically constant along the span and no such secondary motions are set up.

Another particularly attractive feature of the flow over a tapered cylinder is that end effects can be completely eleminated by proper choice of boundary conditions in the spanwise direction. This is in contrast with the linear shear flow case, in which the influence of end conditions cannot be avoided (Mukhopadhyay *et al.* 1999), as shown in the investigation of end effects by Mair & Stansby (1975). This motivates the present computer experiments on flow phenomena in the wake behind a tapered straight circular cylinder in an originally uniform stream.

Three main features of the vortex dynamics in tapered cylinder wakes can be noticed: the characteristic cell pattern, the oblique shedding angle, and vortex dislocation (Williamson 1989) or vortex splitting (Eisenlohr & Eckelmann 1989). Since the earliest work of Gaster (1969), the vortex cell shedding has been proved to be an important characteristic of the vortex dynamics in the wake of a tapered cylinder (Noack *et al.* 1991) and sometimes also of the wake behind a non-tapered straight cylinder (Williamson 1996). Piccirillo & Van Atta (1993) showed that the spanwise of a tapered cylinder could be divided into a certain number of cells. Each cell was characterized by its own constant vortex shedding frequency. This means that two neighbouring cells have their shedding frequencies different from each other. Moreover, the size of the cells could be determined by the variation of the vortex shedding frequency along the spanwise: a sudden change in frequency indicated a change of cell.

After many years of controversy it was pointed out by Williamson (1989), that the oblique shedding behind non-tapered straight circular cylinders was caused by the end effects; i.e. disturbances originating from one end being propagated along the span from one shed vortex to another. For the tapered cylinders, on the contrary, it has been found by Piccirillo & Van Atta (1993) that the vortex shedding pattern was practically unaffected by end conditions. Hence, it seems that the oblique vortex shedding phenomenon of the tapered cylinders has a pure geometric origin. Piccirillo & Van Atta (1993) noticed that the bending of the vortex lines and the vortex splitting phenomenon were linked. A vortex splitting is said to occur when vortex lines of one core split apart to merge into the offset cores of neighboring vortices (Eisenlohr & Eckelmann 1989). The angle between the shed vortices and the cylinder axis was observed to increase from 5° to 25° before the vortex splitting occured. During each split, the vortex lines far away continue to steepen (up to 50°). After the split, the vortex lines again become continuous and slightly inclined with respect to the cylinder axis. They moreover noticed that this vortex lines bending around the vortex split lead to a decrease in the local frequency of vortex shedding.

Table 1: Computer simulations

Case	R_T	l/d_2	d_1/d_2	d_m/d_2	$Re_{d_2}{}^a$	Run
A	100:1	37.473	0.625	0.707	178	14
B	75:1	33.461	0.556	0.631	131	22
C	75:1	33.461	0.556	0.631	163	23

[a] $Re_{d_2} = U.d_2/\nu$, i.e. Reynolds number based on the largest diameter

3 Computational Approach

Piccirillo & Van Atta (1993) considered laminar vortex shedding behind four different circular cylinders with different taper ratios. In this paper computer simulations are reported for three different cases, namely their Run 14 with $R_T = 100:1$ called Case A and their Run 22 and Run 23 with $R_T = 75:1$ called Case B and Case C, respectively. See Table 1 for further details.

Each tapered cylinder was embedded in a 3-D computational mesh with 256 000 points. Based on the results of previous two-dimensional simulations (Vallès *et al.* 2001), this mesh size was found to be the best compromise between cpu-time consumption, storage requirements and resolution. The mesh was divided into 28 blocks. The cross-sectional view in Figure 2 shows how: 6 fine blocks form a ring surrounding the cylinder with 8 coarser blocks outside the first ring in the x-y plane (cylinder cross-section). Two subdivisions were made in the z-direction, i.e. along the cylinder axis.

The parallelized Navier-Stokes solver CBJ (Concurrent Block Jacobi) adopted here is a parallel implicit multiblock time-accurate Navier-Stokes solver, with a coarse-grid correction scheme (CGCS). The CBJ code has been extensively tested and used by Jenssen (1994) and Jenssen & Weinerfelt (1995, 1998) to compute both steady and unsteady flow fields. The full time-dependent Navier-Stokes equations, written in integral form, were solved on the structured multiblock grid. The convective part of the fluxes was discretized with a third-order, upwind-biased method based on Roe's scheme. The viscous fluxes were obtained using central differencing. Derivatives of second-order accuracy are first calculated with respect to the grid indices and then transformed to derivatives with respect to the physical spatial coordinates. Implicit and second-order-accurate time-stepping was achieved by a three-point, A-stable, linear multistep method:

$$\tfrac{3}{2}(V_i/\Delta t)U_i^{n+1} - 2(V_i/\Delta t)U_i^n + \tfrac{1}{2}(V_i/\Delta t)U_i^{n-1} = R(U_i^{n+1}) \tag{3}$$

where the operator on the right-hand side denotes the sum of the flux into volume V_i of the grid cell i,

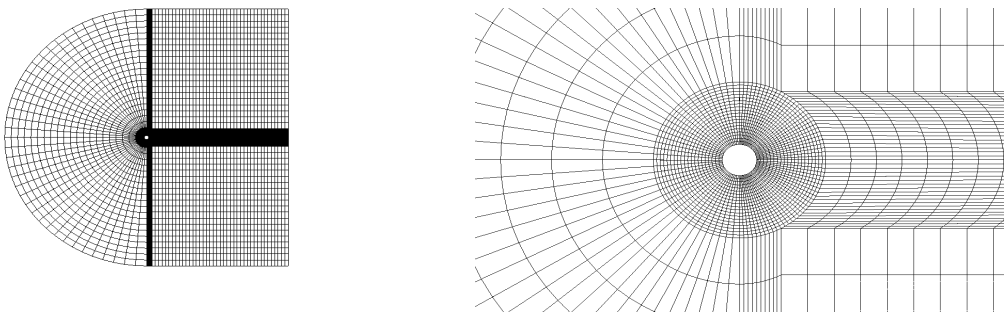

Figure 2: Three-dimensional mesh: view perpendicular to the axis of the cylinder. Left: complete view. Right: close-up.

Δt is the time step and n refers to the time level. To eleminate some of the end effects, Neumann-type boundary conditions were imposed on the $x-y$ planes at the two ends of the cylinder.

The computations were performed on a Cray T3E. The CBJ code ran on 8 processors, each processor handled 32 000 points. The time step was fixed as $0.1d_2/U$, or about 1/50 of the shedding period. Each simulation was run for 500 time steps, i.e. roughly corresponding to ten shedding cycles. The dimensionless convergence criterion for the Newton iteration was 0.001 with a maximum of 20 Newton iterations per time step. The total consumption of cpu-time, after 500 time steps, was approximately 425 hours both for Case A and Case B. This implies an average consumption of 6 cpu sec per grid point, whereas the wall-clock time for each run was approximately 62 hours. Thus, the use of 8 processors in parallel on a Cray T3E enabled each simulation to be completed 7 times faster than on a computer with only a single processor.

4 Results and Discussion

The cellular features of the vortex shedding can be visualized in different ways. Figure 3 gives the time evolution of the pressure field. The pressure values are taken on a line, parallel to the cylinder axis, at $x = 2.5d_m$ and $y = 1d_m$, where d_m is the mean diameter given in Table 1. This detection line was offset $1d_m$ from the cylinder centerline in order to detect only one side of the vortex street. The time-traces to the right in Figure 3 mimicked hot-wire outputs, and from these signals the vortex shedding frequencies at each spanwise location were calculated. By considering the variation in frequency between two neighbouring positions (cf. Section 2), in combination with both visualizations and animations of the flow, the number of shedding cells was determined for each of the three cases.

Instantaneous flow fields are shown in Figure 4. The characteristic cell pattern is clearly visible, both in the isosurfaces of pressure (to the left) and in the isocontours of the spanwise vorticity (to the right). When the end effects at the extremities of the cylinder are discarded, as in the study of Piccirillo & Van Atta (1993), four distinct shedding cells can be identified in Figure 4 for Case B, i.e. fully in accordance with the number of cells seen in the experiment. Although the positions of the cells were not completely fixed, the spanwise locations of the cell centers could be estimated on the basis of the computer simulations. These locations are shown versus local Strouhal number and local Reynolds number in Figure 5 and compared with experimental data for Case B. The results of the computer experiments and the laboratory experiments show the same overall tendency, and the close correspondence between the local Reynolds numbers and the cell center positions are particularly encouraging. The situation is somewhat different for Case A, for which the time histories are shown in the top of Figure 3 and instantaneous flow fields in Figure 4. This flow field appears to be more regular than the two others (Case B and Case C), with the cell positions being gradually shifted in the positive z-direction, i.e. towards the narrow end of the cylinder. The same observation was made by Piccirillo & Van Atta (1993), namely that the flow field tends to be more chaotic with increased tapering (i.e. for lower taper ratios R_T). However, the isobars reveal the existence of 5 distinct cells, in accordance with the observed shift in the vortex shedding frequency, as deduced from the pressure time-histories. This latter finding is in conflict with the three shedding cells observed in the laboratory experiment. Analogous flow visualizations for Case C are shown at the bottom of Figure 3 and in Figure 4. Careful examination of the pressure contours to the left in Figure 3 suggests that a new cell is being created after about 200 time steps about midway between the cylinder ends. Similarly, a new cell is being formed after about 500 time steps. Altogether, four cells are visible at the same time. The experiments suggested that new cells were created near the wide end of the cylinder and gradually shifted towards the narrow end, just as in the present Case A. In Case C, however, the cells formed near the wide end of the cylinder are only shifted spanwise to about $z/d_2 = 15$.

A decade ago, Jespersen & Levit (1991) conducted similar three-dimensional simulations for laminar flow past a tapered cylinder with taper ratio $R_T = 100:1$ in a Reynolds number range from 90 to 145, i.e. somewhat lower than those considered in the present work. Their computations were performed on the massively parallel Connection machine with an implicit, approximate-factorization central-difference

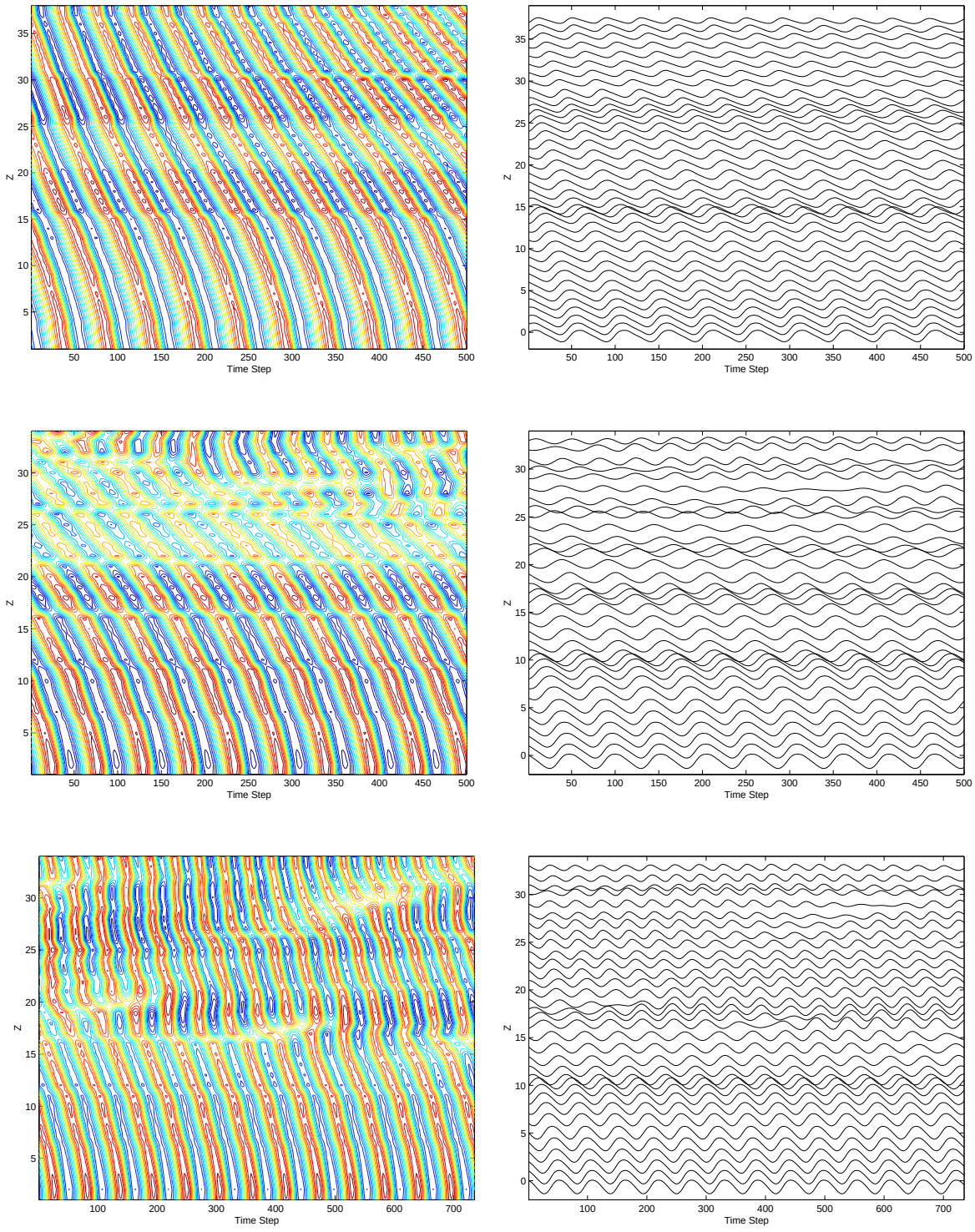

Figure 3: Time evolution of the pressure along the spanwise taken at $x = 2.5d_m$ and $y = 1d_m$. From the top to the bottom: Case A, Case B and Case C. At left, isopressure contours; at right, pressure values at selected spanwise positions.

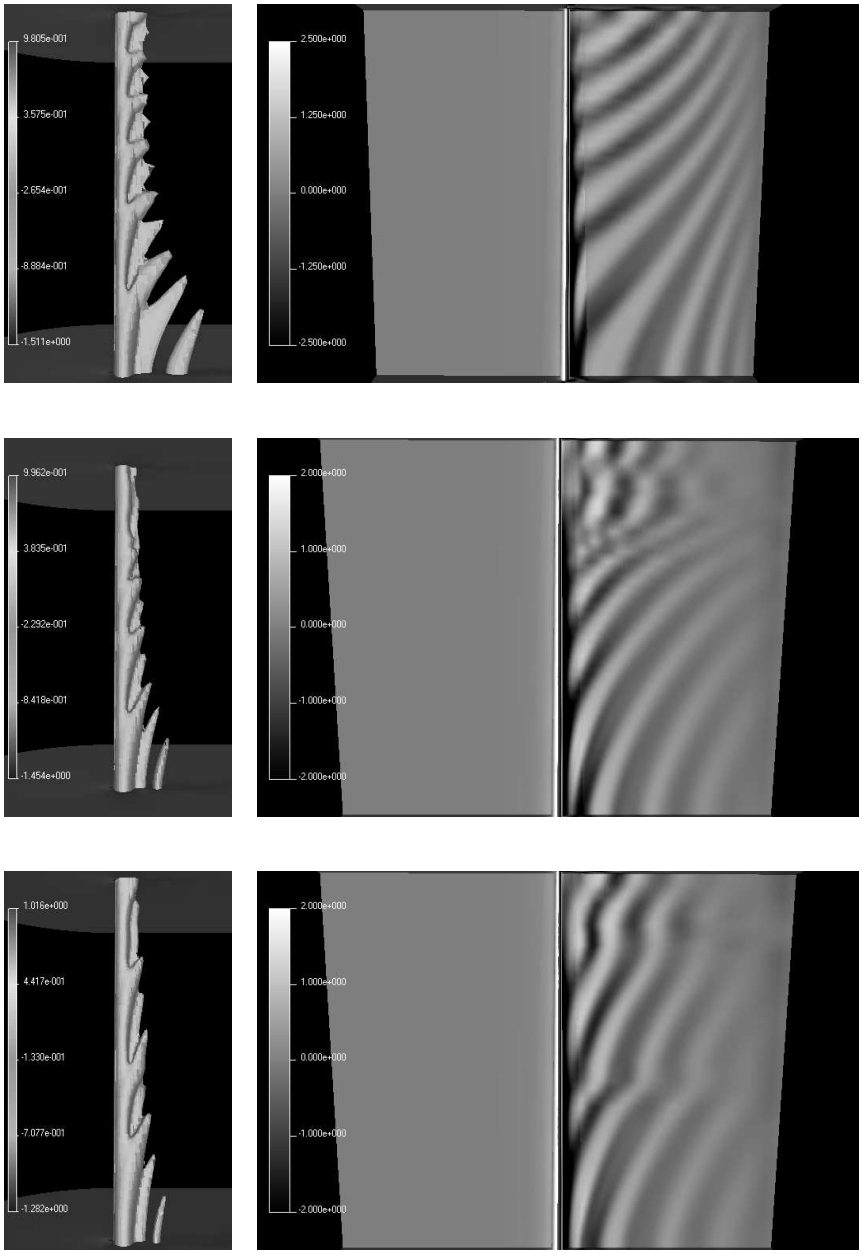

Figure 4: Instantaneous flow field. From the top to the bottom: Case A, Case B and Case C. At left, isopressure surface; at right, spanwise vorticity.

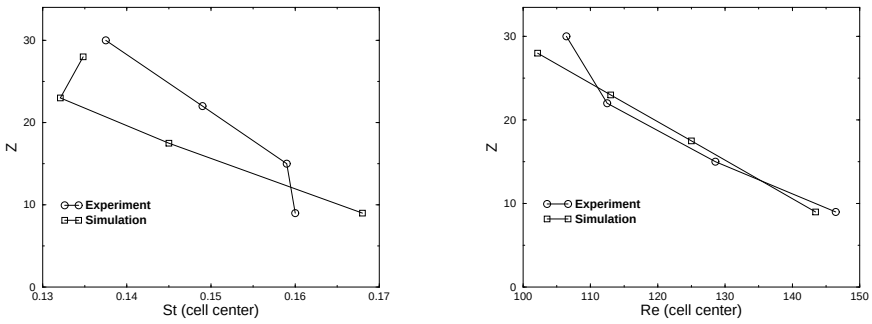

(a) (b)

Figure 5: Cell midpoint locations for Case B (Simulation), compared with experimental data from Piccirillo & Van Atta (1993) (Experiment). (a) versus local Strouhal number, (b) versus local Reynolds number.

code for the full Navier-Stokes equations in generalized curvilinear coordinates and with a three-point implicit second-order time-stepping method.

Their results showed the same qualitative flow behavior as the experiments of Piccirillo & Van Atta (1993) (i.e. velocity-time trace, vortex shedding), but some quantitative comparisons differed, like the number of shedding vortex cells. An interesting result is that they got five cells, i.e. the same as in the present simulation.

The reason why both computer simulations were unable to reproduce the laboratory experiments in every detail is not clear. One explanation could be that the flow past a tapered circular cylinder with high taper ratio ($R_T = 100:1$) is more sensitive to end effects at the extremities of the cylinder than in cases with lower R_T. Indeed, tapered cylinders with taper ratios in the range considered here and by Jespersen & Levit (1991) are not very different from a uniform cylinder, the latter for which Williamson (1989) found that the end cells had very strong effects on the main vortex shedding region. Moreover, Piccirillo & Van Atta noticed that: "For the 100:1 cylinder with $U = 0.5$ cm/s the position of the cell boundaries changed by up to 1.0 cm, when nominally identical runs were compared". Consequently, we ought to state the same conclusion as them, namely that "care must be taken when using the cell boundary positions in quantitative analysis". The same behavior was also described by Monkewitz (2000) during the recent IUTAM Symposium. It is noticeable that in the study of linear shear flow past straight uniform circular cylinders, essentially the same flow phenomena have been observed both experimentally by Mair & Stansby (1975), Stansby (1976) and Griffin (1985) and numerically by Mukhopadhyay *et al.* (1999).

In order to provide further qualitative comparisons, $St(Re)$ curves were plotted in Figure 6. This figure compares the Strouhal-Reynolds relationships deduced from the present simulations with the results of the experiments by Piccirillo & Van Atta (1993). The curve-fit they employed was given by the relation $St_c = 0.195 - 5.0/Re$, where St_c is the Strouhal number associated with an individual shedding vortex cell. The $St(Re)$ relations deduced from the simulations of Case A and Case C are in good agreement with the experimental curve along one half of the cylinders (the narrowest part), i.e. for Re below 150 for Case A and below 115 for Case C; whereas the computations diverge from the experimental results for higher Reynolds numbers. This is mainly due to the fact that the experimental curve is a fit on Strouhal number values taken at the center of each vortex cell only, whereas the present results are based on a truly local Strouhal number for each spanwise location. The difference in spanwise boundary conditions in the experiment and the computations may also explain some of the deviations. A comparison between the simulation conducted by Jespersen & Levit (1991) with $R_T = 100:1$ and the

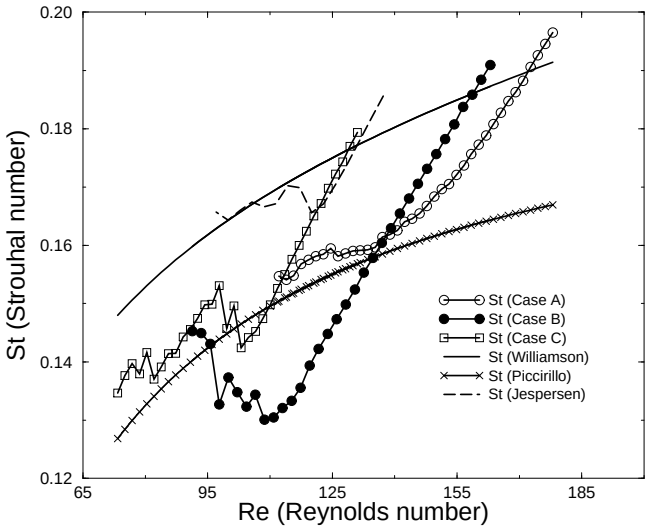

Figure 6: Local Strouhal number (St) versus local Reynolds number (Re). Case A, Case B and Case C refer to the present simulations. Jespersen refers to the simulation with $R_T = 100 : 1$ by Jespersen & Levit (1991). Piccirillo refers to curve fitting of all results reported by Piccirillo & Van Atta (1993). Williamson refers to the universal St-Re curve in equation (1) for straight uniform circular cylinders due to Williamson (1988).

present equivalent Case A in Figure 6, shows that the present results fit quite well with the experimental curve, while those of Jespersen & Levit (1991) are closer to the universal Strouhal-Reynolds number curve for uniform (i.e. non-tapered) cylinders of Williamson (1988). This discrepancy is most likely due to the much coarser grid resolution used by Jespersen & Levit (1991). In conclusion, the present computer simulations showed that the local Strouhal number for tapered cylinders is lower than those for uniform cylinders at the same Reynolds number, fully consistent with earlier observations (Gaster (1969) and Piccirillo & Van Atta (1993)).

The $St(Re)$ relation for Case B, however, seems to be in poor agreement with the experimental results. The only difference between the two simulations Case B and Case C is the Reynolds number based on the wide diameter; cf. Table 1. This modest difference apparently affects the results considerably. By comparing the spanwise vorticity field in planes parallel to the axis of the cylinder in Figure 4(bottom, right) and Figure 4(center, right), a difference near the narrow (upper) end of the cylinder can be observed. In Case B a vortex splitting can be seen. In order to focus on this flow phenomenon, Figure 7 shows a time sequence of the vortex splitting. Considering positive spanwise vorticity (in white), a vortex shedded approximately $l/3$ from the narrow end of the cylinder appears as three white spots on Figure 7(a). The split begins from the "second spot": a part of the main core of the vortex is merging into another vortex. Then, while the process evolves in time and space, carried away by the mean flow, the vortex lines surrounding the split seem to steepen more and more. In Figure 7(d) a second part of the main vortex is splitting to merge into the offset of a second vortex located behind the first one. Finally, in Figure 7(f) a new "main" vortex is shedded from the same location as the first one.

This vortex splitting phenomenon explains what could be seen near the top of the pressure isocontours of Figure 3 (Case B). In the early stage of the process, four areas could be seen until the narrow-end cell began to grow from time step 250, thereby reducing the neighboring shedding cell. Between time step

250 and 300 only 3 cells could be seen. Then from time step 300 to 425 a change occured and 4 areas could again be observed, probably due to a change of phase in the vortex shedding frequency. Finally, from time step 425 until the end of the process, the narrow-end cell considerably reduced its length and a new cell appeared with its center approximately located at the interface between the previous cells.

Hence, the behavior of the $St(Re)$ relation in the Reynolds number range $95-125$ for Case B, i.e. the decrease in local Strouhal number while the local Reynolds number is increasing, is believed to be due to the occurence of the vortex splitting at the narrow end of the cylinder. In fact, the simulation showed exactly the same phenomena associated with the vortex splitting, as stated previously in Section 2, namely a decrease in the local vortex shedding frequency together with a bending of the vortex lines around the vortex split.

In the recent CFD analysis by Mukhopadhyay *et al.* (1999), most of the vortex shedding phenomena described above have been observed. Although they considered flow past a uniform cylinder, their linear variation of the incoming flow u caused a spanwise variation of u/D analogous to that in the present study. Their shear parameter β was equal to 0.02, and according to the relation in Section 2 this corresponds to uniform flow past a tapered cylinder with $R_T = 50:1$. Because this taper ratio is quite different from those involved in the present study, no qualitative comparisons have been made. Nevertheless, their numerical results compared well with experiments by Piccirillo & Van Atta (1993) for a tapered cylinder with $R_T = 50:1$.

5 Concluding Remarks

Accurate numerical solutions of the full time-dependent Navier-Stokes equations have been performed in order to provide an in-depth exploration of the intricate vortex shedding pattern in the wake of linearly tapered circular cylinders. The results for Case A and Case C showed an encouraging consistency with the observations made by Piccirillo & Van Atta (1993). In particular, several important features of the oblique vortex shedding observed experimentally were reproduced by the computer simulations. These include the spanwise variation of the shedding frequency, which gives rise to discrete shedding cells, each with its own shedding frequency. For the tapered cylinder with $R_T = 75:1$, the number of vortex cells, as well as their inclination with respect to the axis of the cylinder, compared with the experiment. The instantaneous vorticity fields mirrored the oblique vortex shedding pattern, whereas the isopressure contours showed that four distinct vortex cells were shed from the cylinder. Animations moreover revealed that the vortex shedding shifts along the span of the cylinder, from the narrow to the wide end. The vortex splitting phenomenon described by Piccirillo & Van Atta (1993) was observed to occur in the wake of the tapered cylinder in Case B. It is noteworthy that the match with the experiments is not uniformly good. For instance, the variation of the Strouhal number along the span matches the experiments only in some of the cases. In other cases the physics of the computed flow field is simply different from that of the laboratory flow and distinct differences in the vortex dynamics are observed for the less tapered cylinders. Finally, striking similarities between uniform flow past tapered cylinders and linear shear flow past uniform circular cylinders were pointed out. The next step of this research programme would be to simulate the turbulent wake phenomena for flow past a tapered cylinder at higher Reynolds numbers, typically $3900 < Re < 5000$, in order to enable comparisons with the experimental study of Hsiao & Chiang (1998). This will be accomplished by means of large-eddy simulations, in which parts of the turbulent fluctuations are accounted for by a sub-grid-scale model.

Acknowledgments

This work has received support from The Research Council of Norway (Programme for Supercomputing) through a grant of computing time. The first author was the recipient of a research fellowship offered by The Research Council of Norway under contract no. 121279/410. The authors are grateful to the referees for some helpful suggestions.

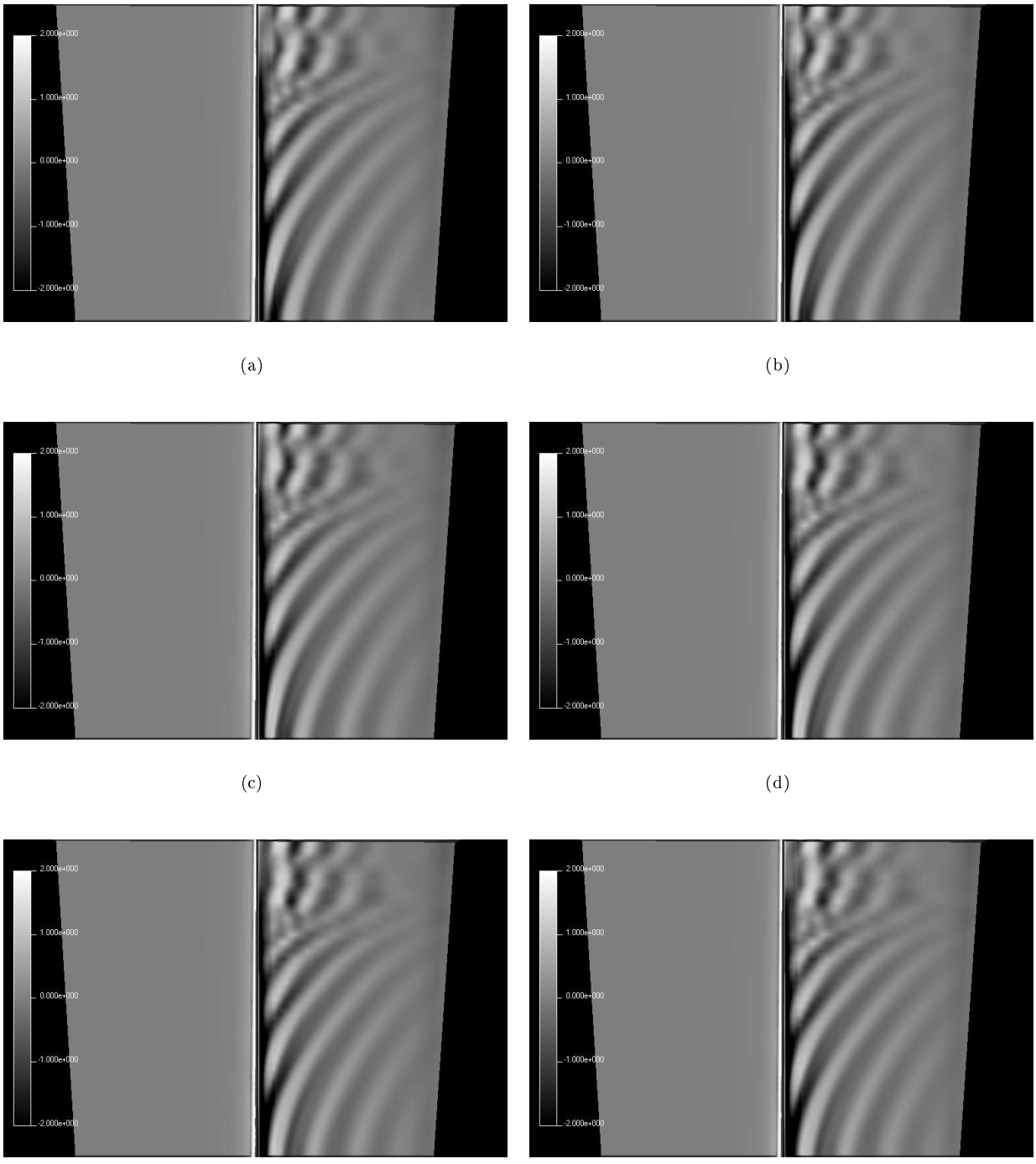

(a) (b)

(c) (d)

(e) (f)

Figure 7: Time sequence of the instantaneous spanwise vorticity showing vortex splitting for Case B. Time step (from the left to the right and from the top to the bottom): (a) 463, (b) 470, (c) 477, (d) 484, (e) 491, (f) 498

References

Eisenlohr, H. & Eckelmann, H. 1989 Vortex splitting and its consequences in the vortex street wake of cylinders at low Reynolds number. *Physics of Fluids* **A 1**, 189–192.

Gaster, M. 1969 Vortex shedding from slender cones at low Reynolds numbers. *Journal of Fluid Mechanics* **38**, 565–576.

Gaster, M. 1971 Vortex shedding from circular cylinders at low Reynolds numbers. *Journal of Fluid Mechanics* **46**, 749–756.

Griffin, O. M. 1985 Vortex shedding from bluff bodies in a shear flow: a review. *Journal of Fluids Engineering (Transaction of ASME)* **107**, 298–306.

Hsiao, F. B. & Chiang, C. H. 1998 Experimental study of cellular shedding vortices behind a tapered circular cylinder. *Experimental Thermal and Fluid Science* **17**, 179–188.

Jenssen, C. B. 1994 Implicit multiblock Euler and Navier-Stokes calculations. *AIAA Journal* **32**, 1808–1814.

Jenssen, C. B. & Weinerfelt, P. Å. 1995 Coarse grid correction scheme for implicit multiblock Euler calculations. *AIAA Journal* **33**, 1816–1821.

Jenssen, C. B. & Weinerfelt, P. Å. 1998 Parallel implicit time-accurate Navier-Stokes computations using coarse grid correction. *AIAA Journal* **36**, 946–951.

Jespersen, D. C. & Levit, C. 1991 Numerical simulation of flow past a tapered cylinder. *AIAA paper* **91–0751**.

Mair, W. A. & Stansby, P. K. 1975 Vortex wakes of bluff cylinders in shear flow. *SIAM Journal on Applied Mathematics* **28**, 519–540.

Monkewitz, P. A. 2000 Modelling of vortex shedding from cylinders with span-wise non-uniformities. Invited lecture at *IUTAM Symposium on Bluff Body Wakes and Vortex-Induced Vibrations*, Marseille France, June 13–16.

Mukhopadhyay, A., Venugopal, P. & Vanka, S. P. 1999 Numerical study of vortex shedding from a circular cylinder in linear shear flow. *Journal of Fluids Engineering (Transaction of ASME)* **121** 460–468.

Noack, B. R., Ohle, F. & Eckelmann, H. 1991 On cell formation in vortex streets. *Journal of Fluid Mechanics* **227**, 293–308.

Papangelou, A. 1992 Vortex shedding from slender cones at low Reynolds numbers. *Journal of Fluid Mechanics* **242**, 299–321.

Piccirillo, P. S. & Van Atta, C. W. 1993 An experimental study of vortex shedding behind linearly tapered cylinders at low Reynolds number. *Journal of Fluid Mechanics* **246**, 163–195.

Stansby, P. K. 1976 The locking-on of vortex shedding due to the cross-stream vibration of circular cylinders in uniform and shear flows. *Journal of Fluid Mechanics* **74**, 641–665.

Tritton, D. J. 1959 Experiments on the flow past a circular cylinder at low Reynolds numbers. *Journal of Fluid Mechanics* **6**, 547–567.

Tritton, D. J. 1971 A note on vortex streets behind circular cylinders at low Reynolds numbers. *Journal of Fluid Mechanics* **45**, 203–208.

VALLÈS, B., JENSSEN, C. B. & ANDERSSON, H. I. 2001 Three-dimensional numerical simulation of laminar flow past a tapered circular cylinder. In *Parallel Computational Fluid Dynamics-Trends and Applications*, C. B. Jenssen *et al.* editors, pp. 581–588, Elsevier Science B. V.

WILLIAMSON, C. H. K. 1988 Defining a universal and continuous Strouhal-Reynolds number relationship for the laminar vortex shedding of a circular cylinder. *Physics of Fluids* **31**, 2742–2744.

WILLIAMSON, C. H. K. 1989 Oblique and parallel modes of vortex shedding in the wake of a circular cylinder at low Reynolds numbers. *Journal of Fluid Mechanics* **206**, 579–627.

WILLIAMSON, C. H. K. 1996 Vortex dynamics in the cylinder wake. *Annual Review of Fluid Mechanics* **28**, 477–539.

WILLIAMSON, C. H. K. & BROWN, G. L. 1998 A series in $1/\sqrt{Re}$ to represent the Strouhal-Reynolds number relationship of the cylinder wake. *Journal of Fluids and Structures* **12**, 1073–1085.

ZDRAVKOVICH, M. M. 1997 *Flow around Circular Cylinders, vol.***1***: Fundamentals.* New York: Oxford University Press.

Appendix D

Appendix D is not included due to copyright restrictions.